M3LW-25OR0402063

Light Water Reactor Sustainability Program

Comparison of IASCC performances of AM-HIP 316, ODS 304, and nanocrystalline 304 alloys

Gokul Subramanian, Arpan Arora, Adam Eichhorn, Stephen S. Raiman
University of Michigan

August 2025

U.S. Department of Energy
Office of Nuclear Energy

M3LW-25OR0402063

Comparison of IASCC performances of AM-HIP 316, ODS 304, and nanocrystalline 304 alloys

Gokul Subramanian
Arpan Arora
Adam Eichhorn
Stephen S. Raiman

University of Michigan

August 2025

Light Water Reactor Sustainability
Materials Research Pathway

http://lwrs.inl.gov

Prepared for the
U.S. Department of Energy
Office of Nuclear Energy

Page intentionally left blank

Summary

This work builds upon established mechanistic knowledge of irradiation assisted stress corrosion cracking (IASCC) in austenitic stainless steels and shifts the emphasis toward mitigating IASCC through engineered microstructures produced by advanced processing routes. We evaluate IASCC with an incremental four-point bend (4PB) test that measured crack initiation as the fraction of irradiated yield strength (%YS) at which cracks first appear. The use of advanced materials requires a modification to our methods. Accurate surface stress determination during bending requires finite-element analysis (FEA), which in turn depends on reliable values for the 320ºC yield strength of both the thin proton irradiated layer and the unirradiated bulk. We have employed high temperature micro indentation to characterize the ion irradiated surfaces, and extract mechanical properties. IASCC testing on a wrought 304L sample irradiated to 5 dpa showed onset of IASCC at 60% of its irradiated yield stress.
Additionally, we report on production and characterization of powder metallurgical 316L and 316L ODS which we believe will be resistant to IASCC.

Acknowledgments

This work was supported by the US Department of Energy, Office of Nuclear Energy, Light Water Reactor Sustainability Program, Materials Research Pathway. The authors acknowledge technical support from the Michigan Center for Materials Characterization, the Michigan Ion Beam Laboratory, and experimental support from Connor Shamberger.

CONTENTS

Acronyms

4PB	4-Point Bend
AM	Additively Manufactured
AR	As Received
BSE	Backscatter Electrons
CAD	Computer-Aided Design
DC	Dislocation Channel
EBSD	Electron Backscatter Diffraction
FEA	Finite Element Analysis
FIB	Focused Ion Beam
GB	Grain Boundary
HIP	Hot Isostatic Press
IASCC	Irradiation-Assisted Stress Corrosion Cracking
IM	Irradiated Materials System
IMTL	Irradiated Materials Testing Laboratory
IR	Infrared
LWR	Light Water Reactor
ODS	Oxide-Dispersion Strengthened
PI	Proton Irradiation
PWR	Pressurized Water Reactor
SEM	Scanning Electron Microscope
SS	Stainless Steel
TEM	Transmission Electron Microscope
UFG	Ultrafine-Grained
WR	Wrought

1. Introduction

1.1 Motivation

Irradiation-assisted stress corrosion cracking of in-core stainless steel components is a critical issue faced by Light Water Reactor (LWR) life extension efforts. As components accrue radiation damage, experience tensile stresses, and are exposed to high-temperature water, intergranular cracks form and propagate in the material. The behavior of core-facing components is critical to economic reactor operation, necessitating a thorough investigation into the mechanisms of IASCC and how it can be mitigated.

1.2 Background

A critical component of IASCC is the formation of dislocation channels. Dislocation channeling is the process by which dislocations in fcc, bcc, and hcp materials clear defects as they move through a slip plane, creating a path from grain boundary to grain boundary for further dislocation motion. Hashimoto et al. [1] showed that high temperature (330 °C) and loss of work hardening are precursors for dislocation channel formation. Dislocation channeling is observed in irradiated materials as a component of irradiation embrittlement caused by nanoscale irradiation defects. As the first dislocations travel on a slip plane to reach the grain boundary, defect clusters are sheared, and work hardening in the channel becomes negligible. McMurtrey et al. showed that slip channels that terminated at grain boundaries were more likely to cause grain boundary cracking, represented in Fig. 1 [2]. It was later shown experimentally by Johnston et al. [3] and computationally by Kuhr et al. [4] that there was a local stress buildup where the dislocations terminated at the grain boundaries but less so when slip channels continued through grain boundaries.

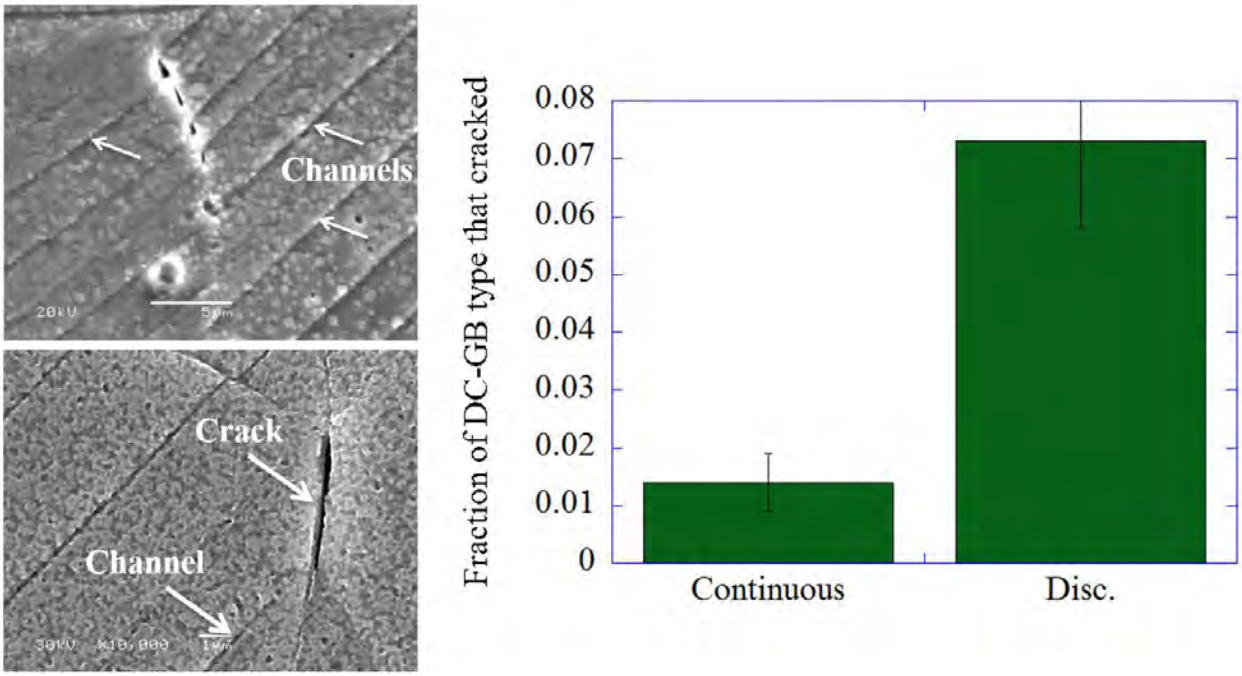

Figure 1: Images of continuous and discontinuous dislocation channels and a histogram showing that discontinuous channels are much more likely to crack. DC: dislocation channel, GB: grain boundary. Images reproduced from [2]

The stress buildup due to dislocation channeling has been shown to act in concert with grain boundary oxidation, known to weaken grain boundaries and promote fracture [5], another key driver of

IASCC [6]. The step height of dislocation channels has also been correlated with IASCC. Austenitic stainless steel (SS) samples with dislocation channel heights measured below a critical value of 300-350 nm did not show IASCC susceptibility in BWR conditions, while samples above that value all experienced IASCC [7]. Jiao et al. explained this critical dislocation height, proportional to the number of glide dislocations in the channel, as the local deformation limit on the dislocation channel to grain boundary interface before the oxide film of the grain boundary ruptures.

1.3 Approach

Researchers at Michigan and worldwide have spent decades building a mechanistic explanation of IASCC [6], including within the LWRS program. Armed with this explanation (partially described in section 1.2), we have begun efforts aimed at IASCC mitigation. The first phase of mitigation efforts targets stainless steels with microstructural features that may make them resistant to dislocation channeling. Three engineered microstructures were chosen. First, an ODS 304L SS is anticipated to resist dislocation channeling by oxides acting as pinning points, preventing channel formation. Second, an ultrafine-grained (UFG) 304L SS, produced by equal channel angular extrusion, has a high grain boundary density predicted to resist dislocation motion and prevent channeling. Third, an additively manufactured and hot isostatically pressed (AM-HIP) 316L SS has been shown to exhibit broad dislocation channels that result in reduced local strain at grain boundaries (GBs) [8]. These microstructures are shown schematically in Fig. 2.

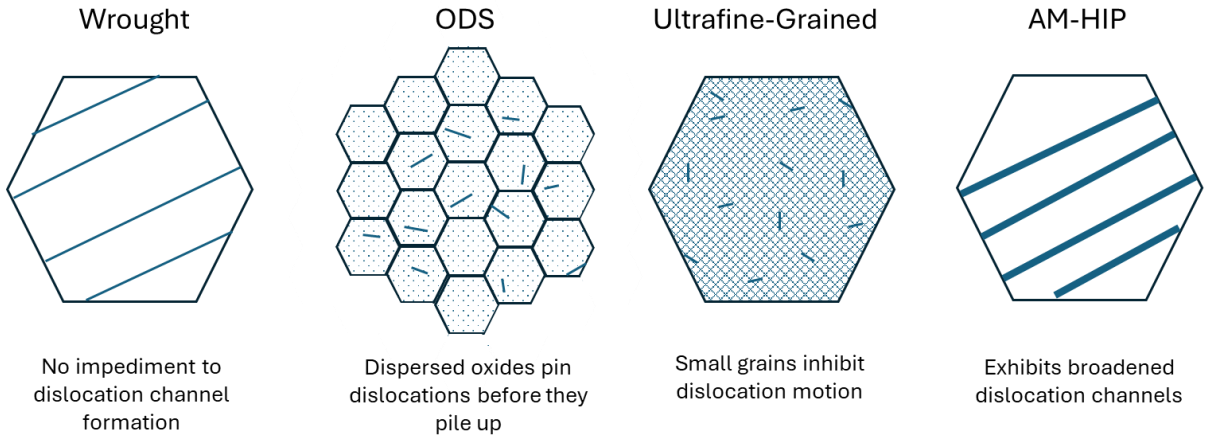

Figure 2: A schematic explanation of the IASCC-resistant microstructures to be examined within this work.

Along with transitioning from understanding IASCC mechanisms to exploring mitigation techniques comes a shift in how experiments must be conducted. While previous experiments used neutron-irradiated samples taken from commercial or test reactors, no such specimens exist for the novel alloys employed by this new mitigation effort. Therefore, samples will be irradiated in-house at the Michigan Ion Beam Laboratory before testing for stress corrosion cracking in LWR conditions. A comparison of neutron and proton irradiated samples is shown in Fig. 3. The purple and the red curves represent stress strain behavior of the neutron and proton irradiated regions, respectively. However, for proton irradiated specimens, the irradiated layer is thin, and the bulk of the sample is non-irradiated and the stress-strain behavior of the whole sample is dominated by the non-irradiated portion of the sample, depicted in light blue. For this reason, efforts in this FY have been aimed at measuring the mechanical properties of the thin irradiated region and modeling the behavior of the coupled irradiated-non-irradiated sample, so we can extract meaningful IASCC data from these samples.

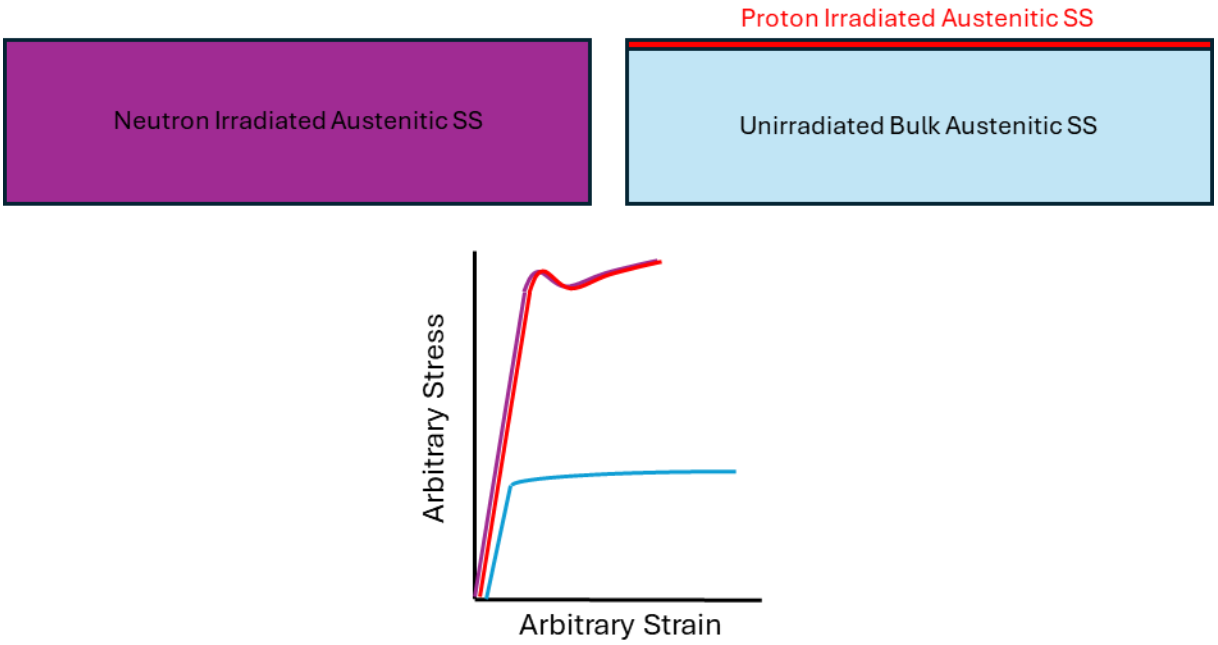

Figure 3: Comparison of stress strain curves for neutron and proton irradiated samples.

A key transition in 4-point bend (4PB) testing is the shift from neutron-irradiated materials to proton-irradiated samples. Proton irradiation presents several advantages for IASCC testing, including faster, more consistent, and cost-effective radiation damage accumulation while significantly reducing radiation exposure to research personnel. The 2 MeV proton irradiation results in radiation damage concentrated within the top 20 μm of the surface layer, sufficient for IASCC initiation studies. Furthermore, IASCC testing of proton-irradiated samples is expedited due to the softer bulk material beneath the irradiated layer, allowing the target surface stress to be achieved more rapidly.

However, a notable challenge in utilizing proton-irradiated 4PB samples for IASCC testing is the complexity of determining the effective surface stress on the proton-irradiated convex bend side. The mechanical behavior of the soft bulk material differs significantly from that of the irradiation-hardened surface layer. The yield strength of the irradiation-hardened layer is approximately four times greater than that of the as-received material, leading to early yielding and permanent plastic deformation in the bulk, even when the surface stress is well below the yield stress. Upon unloading, the entire 4PB sample remains bent, with the entirety of the plastic deformation occurring in the softer bulk. Thus, the surface layer remains elastically bent at loads lower than its yield stress. In contrast, neutron-irradiated samples typically exhibit uniform irradiation hardening throughout the sample, allowing them to behave as a single elastic body below the surface yield stress. As a result, the estimation of surface stress in neutron-irradiated samples was relatively straightforward, with a linear relationship between the applied load and effective stress [9].

After irradiation, the performance of each microstructure will be evaluated using 4PB testing in PWR water at 320 °C. Since proton irradiation cannot uniformly irradiate the samples' thickness, a finite element analysis (FEA) model is employed to interpret the results of 4PB testing.

In this work, we discuss recent progress toward our goal of measuring IASCC in alloys with engineered microstructures designed to resist IASCC. We will describe proton irradiation experiments, and preparation for novel 4-point bend IASCC testing on proton irradiated samples, made necessary by using these new alloys.

1.4 Sample History

Samples were sourced from researchers at the University of Nebraska–Lincoln, researchers at Purdue University, and the Yuen Chang Stainless Steel Corporation. The ODS 304L SS provided by the University of Nebraska was fabricated by spark plasma sintering and is described in [10]. The UFG 304L SS was manufactured at Taxes A&M University by equal channel angular pressing to reduce grain size to 0.1 µm [11]. The AM-HIP 316L SS was provided by Dr. Xiaoyuan Lou at Purdue, and was manufactured from commercial powder using laser powder bed fusion and processed using a hot isostatic press [8]. The wrought (WR) 304L was purchased from the Yuen Chang Stainless Steel Corporation, where it was cold rolled. The compositions of each material are given in Table 1, as reported by the providing institutions.

Table 1: Composition of AM-HIP, ODS, UFG, and WR samples.

Element (wt %)	Fe	Cr	Ni	Si	Mn	Mo	Co	C	N	Y_2O_3	Ti	W
AM-HIP 316L SS	Bal.	17	10	1	2	2.5	-	0.03	0.1	-	-	-
ODS 304L	Bal.	18	8.5	-	-	-	-	-	-	0.35	0.5	2
UFG 304L	Bal.	18.19	8.04	0.3	1.68	0.12	0.16	0.02	0.08	-	-	-
WR 304L	Bal.	18.09	8.01	0.41	1.43	0.03	-	0.025	0.072	-	-	-

Samples were irradiated previously at the Michigan Ion Beam Laboratory and the irradiation conditions are shown in Table 2. The temperature and pressure were steady throughout the experiment. The standard deviation for the temperature is slightly larger than expected because of the temperature of one irradiated specimen wandered out of range during the irradiation, but that sample is not shown in this work. The stage current held at 23 µA throughout the experiment.

Table 2: Irradiation conditions

	Target	**Achieved**
Damage Level (dpa)	**5**	**5**
Damage Rate (dpa/s)	**8.42×10^{-6}**	**8.34×10^{-6}**
Temperature (°C ± 2σ)	**360**	**359.3 ± 8.8**
Chamber Pressure (torr)	**8×10^{-8}**	**(3×10^{-8}, 3×10^{-7})**

1.5 Four-Point Bend Test Geometry

For the 4PB test, as shown schematically in Fig. 4, samples with dimensions of 5 x 3.5 x 2 mm were prepared from the as-received material plates or blocks using electrical discharge machining technique. The 4PB samples from the WR 304L plate were machined such that the longitudinal axis of the sample was aligned with the rolling direction, while the transverse axis corresponded to the long transverse direction (see Fig. 4). Both sides of the short transverse direction of the samples were ground and polished to achieve a final thickness between 0.8 and 0.9 mm. For all samples, the side intended for irradiation was finely polished. The WR 304L sample was electropolished in a 10% perchloric acid 90% methanol solution at –45 °C. However, electropolishing did not produce the desired surface finish for other samples, which were instead vibratory polished using 0.04 µm colloidal silica as a final step. Due to its combined chemical-mechanical effects, vibratory polishing has been reported to yield a damage-free surface layer [12].

Guide bars of 304L steel were ground to the final thickness of 0.9 mm and polished on the short transverse direction to 1200 grit. These bars, cut by electrical discharge machining to 12 x 2 x 1.5 mm before final grinding, provide surfaces on which thermocouples could be welded to monitor the samples between them.

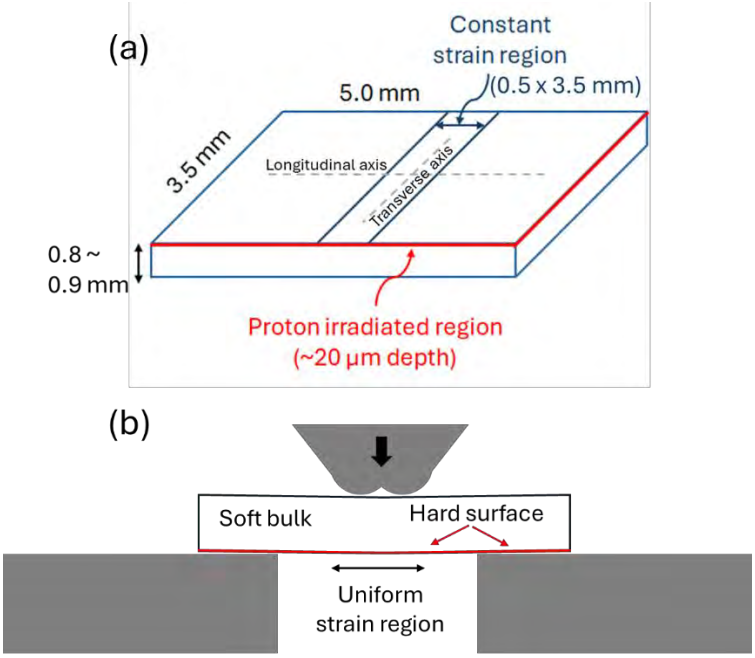

Figure 4. Schematic of (a) proton-irradiated 4PB test specimen and (b) 4PB testing method

2. Property Measurement

One challenge with the switch from neutron irradiation to proton irradiation is measuring the high-temperature mechanical properties of the irradiated specimens. The thin irradiated layers, around 20 μm, cannot be characterized by traditional methods, and no literature data exists for the high-temperature yield strength of the materials with novel microstructures, let alone their yield strengths at high temperatures after irradiation. Despite the lack of data, these are key inputs for the FEA model and are necessary for conducting proper 4PB tests. IASCC tests will be conducted at 320 °C in PWR water, necessitating material property data at this temperature for a more accurate simulation of sample bending.

To determine the surface stress level, a FEA model was developed using the ANSYS Workbench program. This model was originally created for another project which utilized a similar test methodology. The model's setup and element size settings are shown in Fig. 5. The model requires material properties at the 4PB test temperature of 320 °C, including the yield strength, strain hardening coefficient, Young's modulus, sliding friction coefficient, density, and Poisson's ratio for both the unirradiated bulk and the irradiated surface layer. While most of these parameters can be obtained from literature, the yield strength is a particularly critical input for both the FEA simulation and the subsequent determination of the IASCC failure stress. Using the provided material properties, the FEA model calculates stress, strain, and deflection profiles on the sample surfaces. The model was then validated against experimentally determined surface strain and specimen deflection data from tests on blank unirradiated specimens. Because the model's output is dependent on specimen thickness, individual FEA simulations are required for each 4PB specimen.

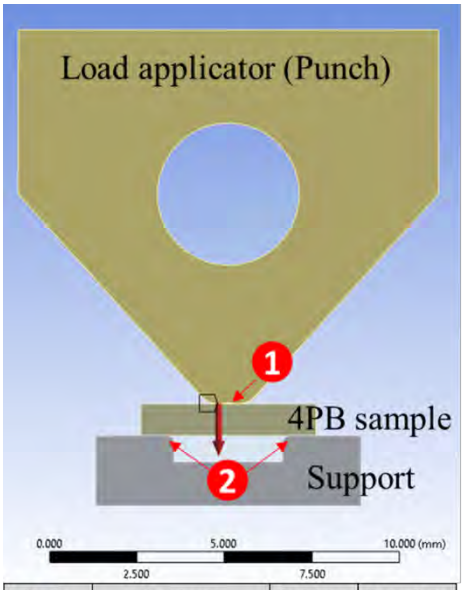

Position	Contact parts	Contact type	Friction factor
1	Load applicator – specimen back surface	Frictional	0.55
2	irradiated surface – base (support)	Frictional	0.55

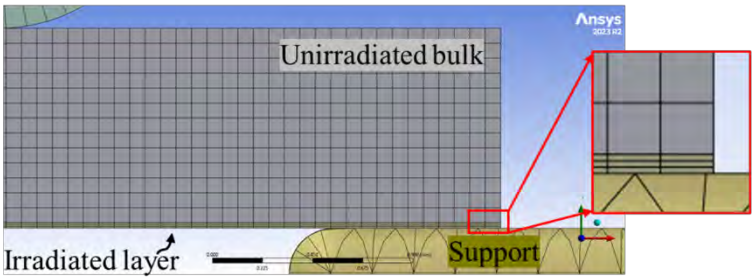

Body	Number of elements layers	Element dimension (mm x mm x mm)
Bulk	13	0.07 x 0.07 x 0.07
Proton-irradiated layer	3	0.07 x 0.07 x 0.01

Figure 5. Schematic 4PB setup for FEA and mesh size settings showing number of element layers and dimensions for the unirradiated bulk and irradiated layer.

For unirradiated wrought materials available in sufficient quantities, it is straightforward to obtain yield strength by performing tensile tests. However, for other engineered alloys fabricated in small quantities, the fabrication of tensile specimens is not possible. A similar situation exists for the determination of the yield strength of the thin proton-irradiated layer. In these cases, it is necessary to rely on the hardness–yield strength correlation, as material hardness can be determined more easily. In this study, Berkovich micro-indentation was performed at room temperature, 320 °C, and 340 °C to calculate the bulk hardness values. Yield strength data is available for some of the unirradiated alloys and from the literature for comparable neutron-irradiated materials. The objective is to compare the yield strength and hardness for the materials with existing data for both properties, and subsequently to estimate the yield strength from hardness for the remaining materials.

2.1 Materials

Table 3 summarizes the alloys used in this study, their processing and irradiation conditions, and the test matrix. Several wrought alloys were previously tested at 340 °C for another study and their relevant yield strength results are available for comparison in this work. Although the 304L-UL and 304L-UR are essentially the same alloy, the 304L-UR samples were sourced from specific locations within the wrought plates, with a tight positional tolerance through the plate depth. All wrought alloys were received in plate form after having undergone a solution annealing treatment. In this study, proton-irradiated samples were available only for the 304LN-RR, 316L AM-HIP, and 304L ODS alloys.

Table 3. *Test alloys, processing and irradiation conditions, and their test matrix.*

Material processing[1]	**Alloy**	**Irradiation condition**[2]	**Berkovich bulk hardness (GPa)**			**Tensile test YS (MPa)**		
			RT	**320 ºC**	**340 ºC**	**RT**	**320C**	**340C**
Wrought	304L-UL	UI	✓	✓		✓	✓	
	304L-UR	UI	✓	✓	✓	✓		✓
	304L-RR	UI	✓		✓	✓		✓
	304LN-RR	UI	✓		✓	✓		✓
		PI	✓	✓	✓			
AM-HIP	316L AM-HIP	UI	✓	✓				
		PI	✓	✓				
ECAP	304L UFG	UI	✓	✓		✓	✓	
SPS	304L ODS	UI	✓	✓				
		PI	✓	✓				

[1]AM-HIP: Additive-manufacturing hot isostatic pressing, ECAP: equal channel angular pressing, SPS: spark plasma sintering
[2]UI: unirradiated, PI: proton-irradiated

2.2 Micro-indentation

A Hysitron TI 950 TriboIndenter was used to determine the bulk hardness values in this study. The instrument is equipped with a standard transducer (load < 10 mN) and a high-load transducer (load < 12 N). The standard transducer is ideal for nano-indentation analysis, while the high-load transducer is required for micro-indentation. Since Vickers hardness measurements at 25 gf (245 mN) are typically used to measure hardness within the proton-irradiated layer, performing micro-indentation in this load range is a valid approach. A diamond Berkovich probe was used for all tests, which has good thermal stability for use at temperatures around 350 ºC. A key benefit of micro-indentation is that the maximum indentation depth on the proton-irradiated samples is approximately 2 µm, which covers a reasonable sampling volume within the 20 µm irradiated layer. In contrast, nano-indentation typically results in depths of up to a few hundred nanometers. While ideal for thin heavy-ion irradiated layers, this depth range covers only a small fraction of the thicker layer in proton-irradiated samples (Fig. 6a).
While Vickers hardness testing of proton-irradiated samples uses a constant load in a typically low range (~ 25 gf), direct comparison with results from neutron-irradiated samples which use much higher loads (often well above 300 gf) is challenging due to the indentation size effect (ISE). The ISE dictates that at shallower depths resulting from lower loads, the measured hardness values are higher. Hardness then

decreases with increasing depth before settling to a near-constant, load-independent value. This effect is attributed to the higher density of geometrically necessary dislocations required to accommodate deformation in smaller volumes, which increases the material's apparent flow strength. It is therefore critical to estimate the load-independent hardness (bulk hardness) to properly utilize existing hardness-yield strength correlations. It is experimentally feasible to determine the bulk hardness by plotting hardness versus depth (Fig. 6b) and extrapolating the data using the Nix-Gao method[13].

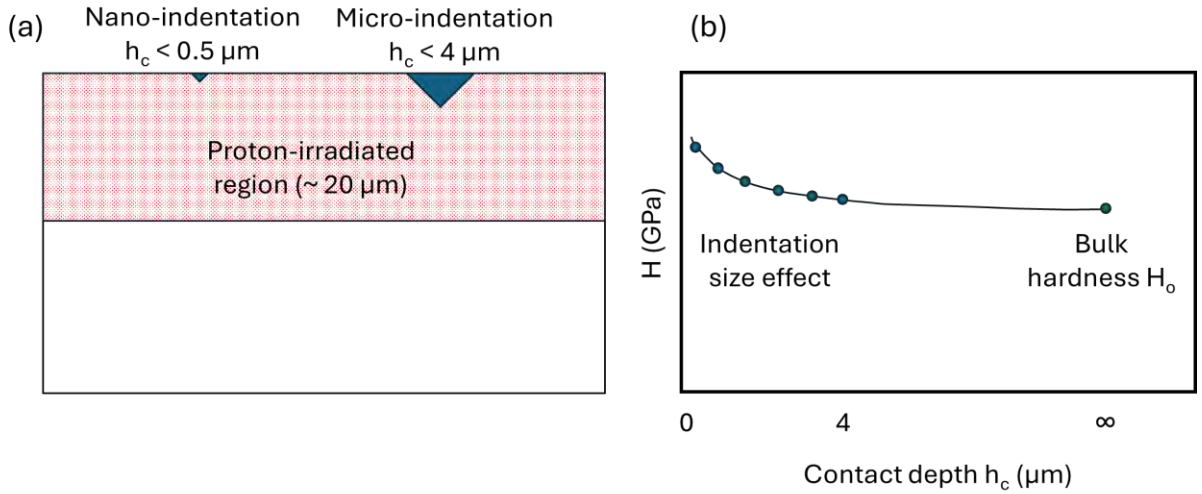

Figure 6. *Schematic of (a) nano- and micro-indentation depth ranges on proton-irradiated layer and (b) example of hardness decrease as a function of depth.*

Hardness can be calculated from the unloading segment of an indentation load-displacement curve using the Oliver-Pharr method[14]. In a conventional single indentation test, which contains only one loading and unloading segment, only a single hardness value can be extracted from each location. This approach requires a wide testing area on the sample to generate a complete hardness vs. depth plot (Fig. 6a), consuming valuable space within the compact, constant-strain region of the 4PB sample that is needed for observing IASCC initiation sites (Fig. 4). An alternative is the multiple-partial unloading technique, where several loading and partial unloading segments at different holding loads are included in a single, complete indentation cycle[15]. The multiple unloading segments in the load-displacement plot enable numerous hardness values to be extracted at different depths from a single indentation site (Fig. 6b). This makes it possible to obtain a complete hardness vs. depth dataset from just a few indentations, providing substantial data while preserving sample area and saving time. It has been reported that the multiple-partial unloading technique yields results comparable to the conventional single unloading technique for a variety of materials[15]. In this work, these two indentation techniques are compared in the load range of 50–500 mN for the unirradiated alloys using a standard room-temperature stage setup. For the multiple-partial unloading indentation technique, 10 loading and partial unloading-cycles were performed where the unloading is down to 50% of the last loading force. The multiple-partial unloading indentations were performed in load-controlled mode, with each partial cycle consisting of a 5 second loading segment, a 2 second holding segment, and a 5 second unloading segment. The process is shown schematically in Fig 7.

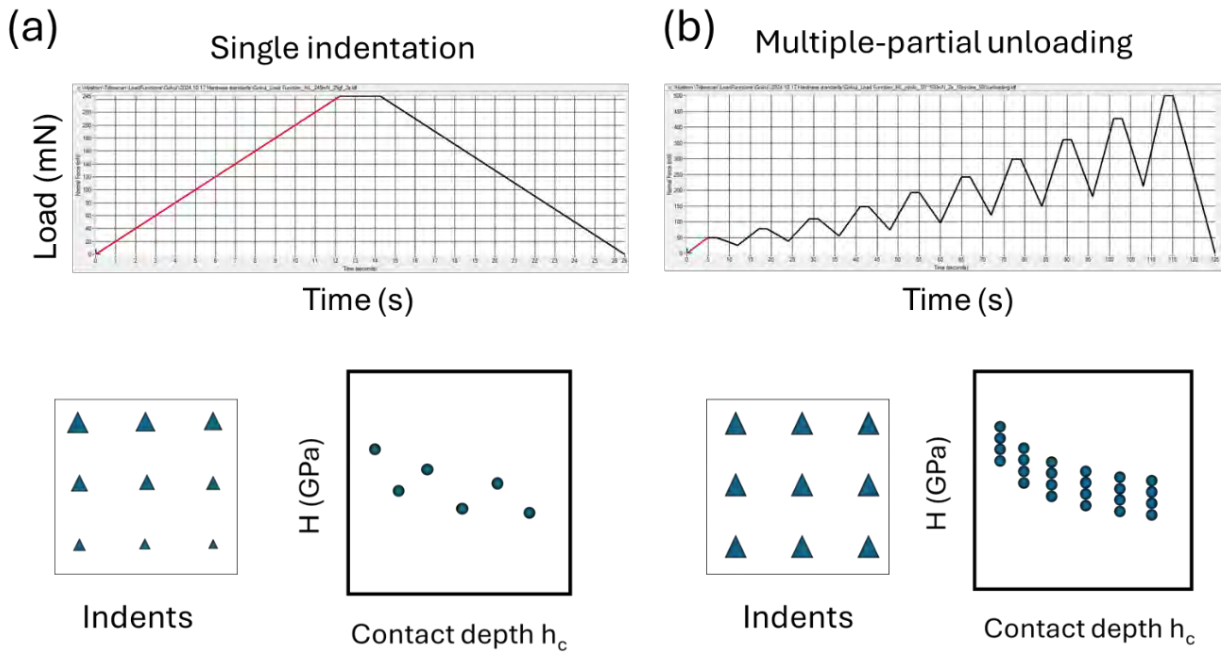

Figure 7. Comparison of (a) single indentation and (b) multiple-partial unloading technique.

A Bruker xSol 600 high-temperature stage was used for performing micro-indentation at 320 °C and 340 °C in an Ar environment. For testing, the 4PB samples were sandwiched between top and bottom plates using spring clips. Both plates contained a heater and were in direct contact with the sample. Temperature sensors were located inside both heaters, which were surrounded by ceramic insulators. This setup created a controlled micro-environment with an Ar atmosphere for high-temperature indentations. Heat transfer calculations show that the temperature at the indentation location is within 1 °C of the measured sensor temperatures. A hole in the top plate allowed an extended probe with the Berkovich tip to access the sample and perform the indentation. The Berkovich tip was located at the end of a long glass shaft to provide thermal insulation for the sensitive electronics at the other end.

The experimental procedure began with setting up the stage and establishing a stable Ar flow. The sample was then heated at a rate of 10 °C/min to the target test temperature of 320 °C or 340 °C. Once the target temperature was reached, the system was held for 10 minutes to stabilize. The indenter tip was then brought close to the sample surface, where it was held for an additional 5 minutes to achieve thermal equilibrium followed by thermal drift measurement for 2 minutes and the indentation program. Several indentations were performed on each sample. To ensure reliable and directly comparable measurements, only data collected using this specific setup and probe at both room and high temperatures were considered for the final analysis.

2.2.1 Multiple-partial unloading:

Representative load-displacement plots for a single indentation test and a multiple-partial unloading test are shown in Figs. 8a and 8b, respectively. The hardness values were calculated for each unloading segment using the Oliver-Pharr method[14]. A series of tests, including both single indentations at various holding loads and multiple-partial unloading indentations, were performed on the unirradiated 304L-UL and the engineered alloys using the standard room temperature indentation stage setup. The corresponding hardness-contact depth profiles are shown in Fig. 9. The results show that the hardness-depth profiles obtained from both techniques agree, which validates the use of the multiple-partial

unloading technique for determining the complete hardness-depth profile. This direct comparison could only be made at room temperature due to the limited accessible sample area within the high-temperature indentation setup, a constraint imposed by the dimensions of the hole in the top plate that allows access for the indenter probe.

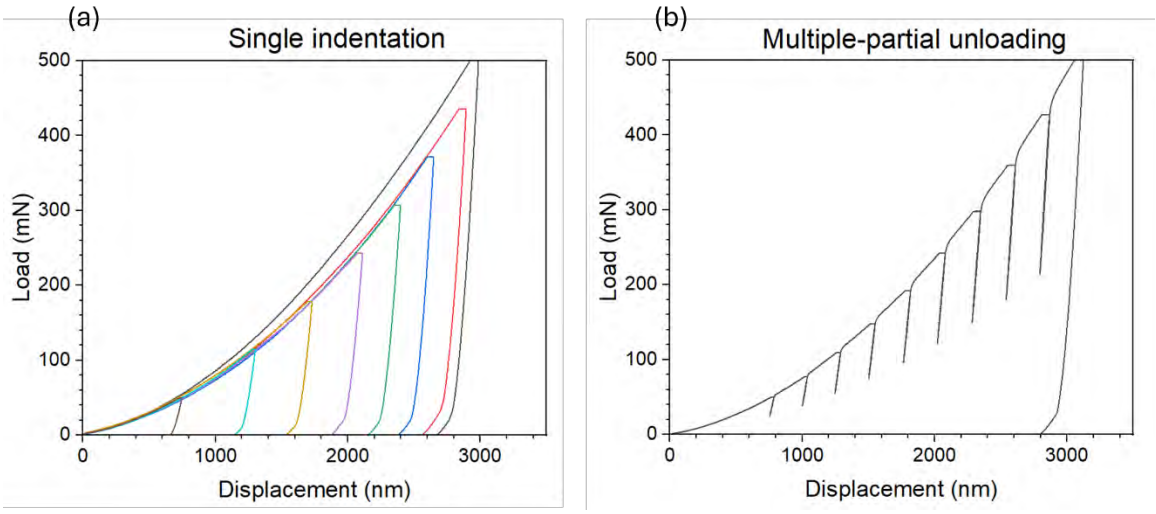

Figure 8. Examples of load-displacement plots from (a) single indentation and (b) multiple-partial unloading techniques in unirradiated 304L-UL specimen.

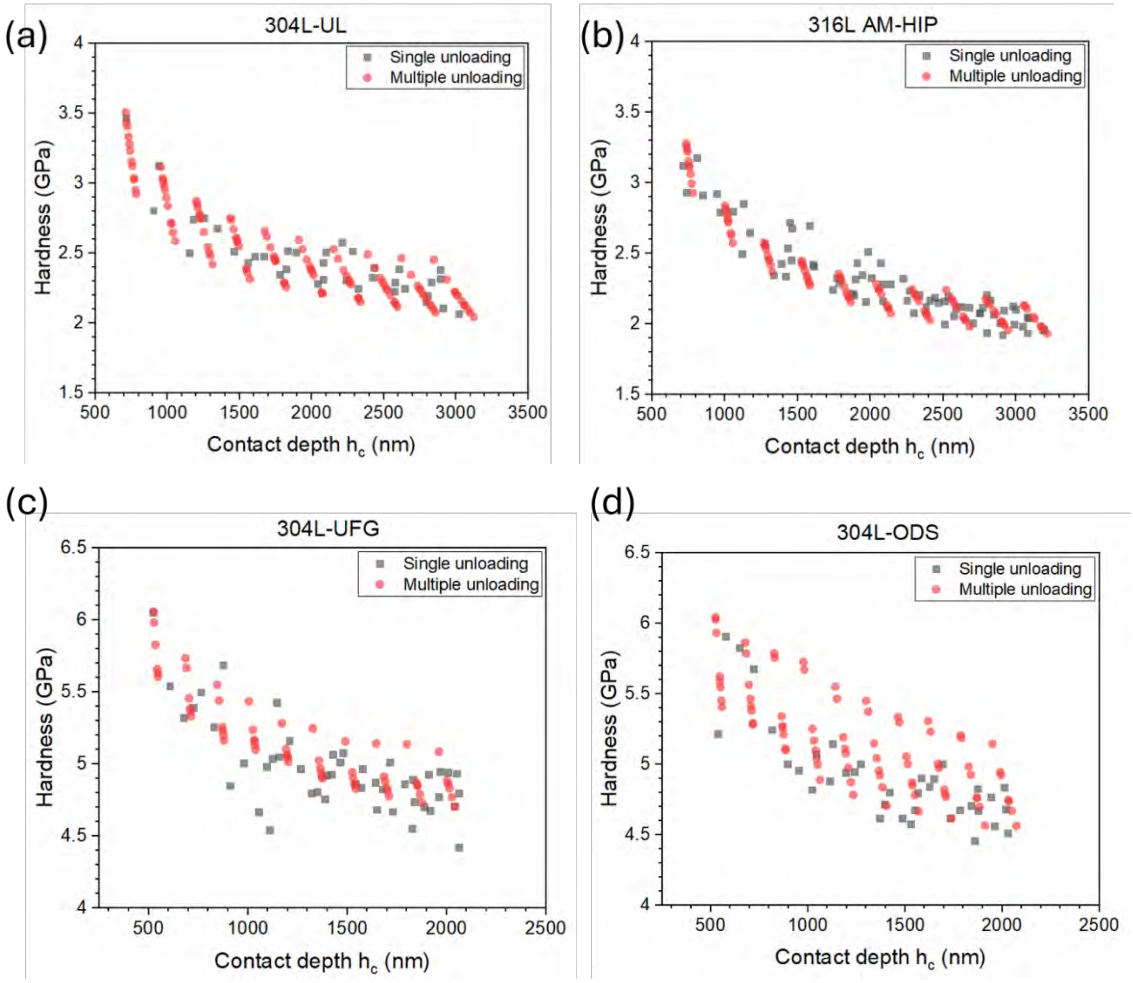

Figure 9. Hardness-depth profiles from single indentation and multiple-partial unloading of (a) 316L-UL, (b) 316L AM-HIP, (c) 304L UFG, and (d) 304L ODS alloys.

2.2.2 Effect of load rate

The multiple-partial unloading indentations were performed entirely in load-controlled mode. This method constitutes multiple cycles, with each cycle having a different effective load rate, which could potentially affect the reliability of the calculated hardness values. To investigate the effect of the load rate, three separate single indentation tests were performed at 340 °C using different loading and unloading durations: 15, 60, and 120 seconds for each segment. This range was chosen to closely match the effective load rates present in the multiple-partial unloading indentations. As shown in Fig. 10, the corresponding load-displacement plots overlap closely and yield similar hardness values, suggesting that the load rate does not have a significant effect on the results within this range.

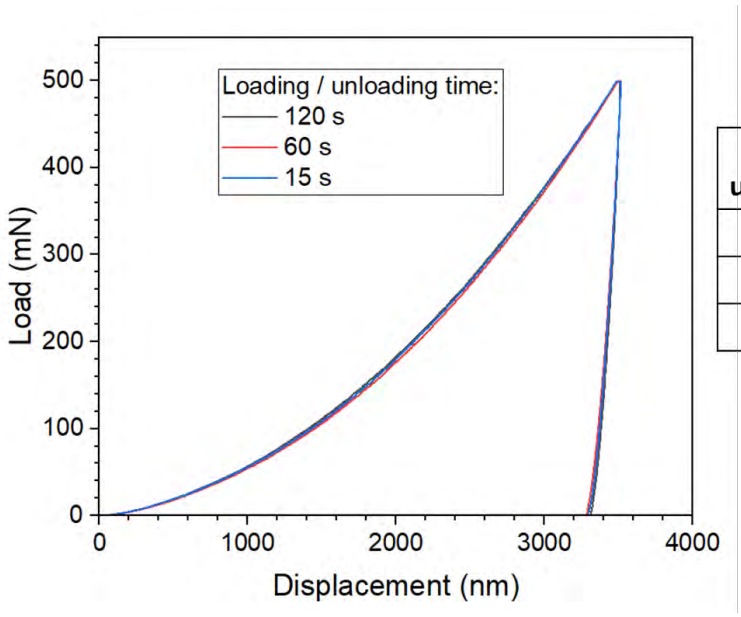

Loading / unloading time	Hardness (GPa)
120 s	1.77
60 s	1.79
15 s	1.78

Figure 10. Load-displacement plot and corresponding hardness values at different load rates for unirradiated 304LN-RR specimen at 340 °C.

2.2.3 Drift correction

During micro-indentation at high temperatures, thermal drift of the probe or stage frame can occur. This may introduce large errors in the displacement values and in turn affect the accuracy of the hardness calculation. To account for this, the TriboIndenter system was set to monitor the Z-axis drift rate of the probe for 2 minutes at 320 °C and 340 °C before the start of each indentation. The drift rate (in nm/s) measured at the end of this monitoring segment is then held constant and used to apply a linear correction to the displacement data of the entire curve. While in most indentations the measured drift rate was very low and resulted in well-formed load-displacement curves, in a few cases particularly during the later stages of high-temperature testing the measured drift was considerable. This caused the resulting load-displacement curves to shift relative to other indentations and do not overlap well. Furthermore, a mismatch between the unloading and reloading segments appeared in each cycle for these cases, despite the drift correction applied by the TriboIndenter software.

It is understood that the standard drift correction is sometimes imperfect because the actual drift rate changes throughout the indentation, deviating from the single, initially measured value. Interestingly, when the pre-measured drift rate is minimal, the load-displacement plot appears well-formed. However, if the measured drift rate is considerable, a shift appears between the unloading and reloading segments and in the overall curve. This can be observed in Fig. 11a in which the middle curve shows no mismatch and corresponds to a very low initial drift rate of –0.16 nm/s. When the drift rate is positive as in the case with a value of 3.64 nm/s, the reloading segment lies before the unloading segment in the load-displacement curve, which corresponds to an overcorrection of the displacement drift. The opposite occurs for a negative drift rate as in the case of –4.17 nm/s, where the reloading segment lies after the unloading segment corresponding to an undercorrection.

Fortunately, the multiple-partial unloading technique enables the direct observation of these drift effects within the load-displacement plot, and the mismatch between the unloading and reloading segments can be utilized for a more accurate drift correction. We observed that for load-displacement plots with very low initial drift rates and well-formed curves, zooming in on the transition between the unloading and

reloading segments shows a very close match, although a minor hysteresis loop is still present (Fig. 12a). Within this loop, the segments were found to overlap at a load corresponding to an average of 0.98±0.01 times the previous holding load, which is consistent at both room and high temperatures.

Subsequently, a Python code was developed to analyze the indentation data files. The code identifies the unloading and reloading segments and calculates the displacement offset between them at a load equal to 0.98 times the previous holding load and correspondingly the local drift rate. This drift rate was plotted as a function of time and then fitted with a linear, second-order polynomial, or exponential function based on the best fit (Fig. 12b). The resulting fitting equation was then used to apply a new, dynamic drift correction to the original load-displacement data to generate a corrected curve.

The results of this new procedure are shown in Fig. 11b, which displays the corrected versions of the three divergent load-displacement curves from Fig. 11a. The drift correction performs exceptionally well, as the previously mismatched curves now show very close overlap and have nearly identical load-displacement profiles. The value of this method is further evidenced in Fig. 11c, which shows several varied and mismatched load-displacement plots from a single test. After applying the new drift correction, these same plots as shown in Fig. 11d form a very tight data cluster with reduced variation. Therefore, all load-displacement curves considered for the analysis in this work were corrected using this method.

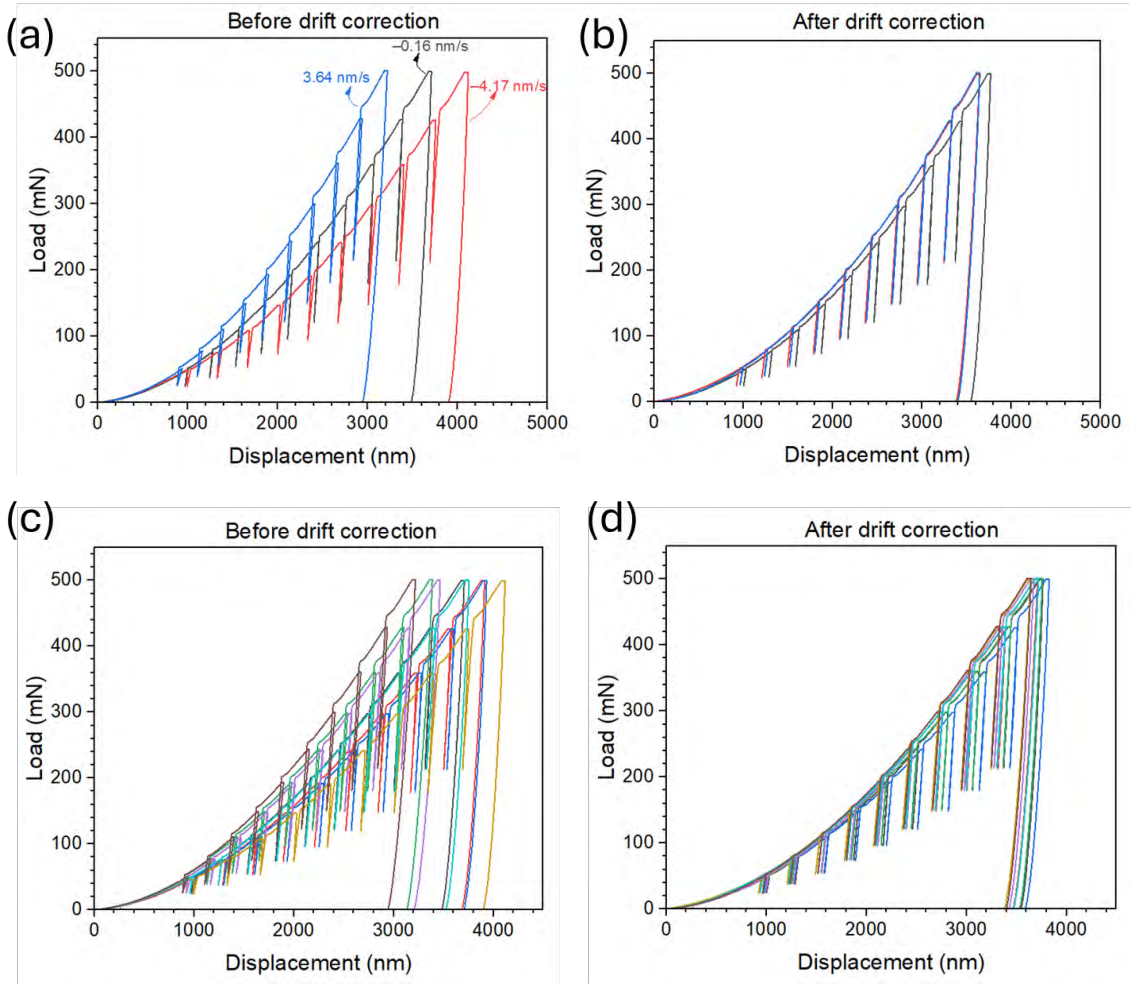

Figure 11. Comparison of load-displacement plots for unirradiated 304L-RR samples tested at 340 °C. (a) and (c) show the indentation data before drift correction, while (b) and (d) show the same data after the custom drift correction has been applied.

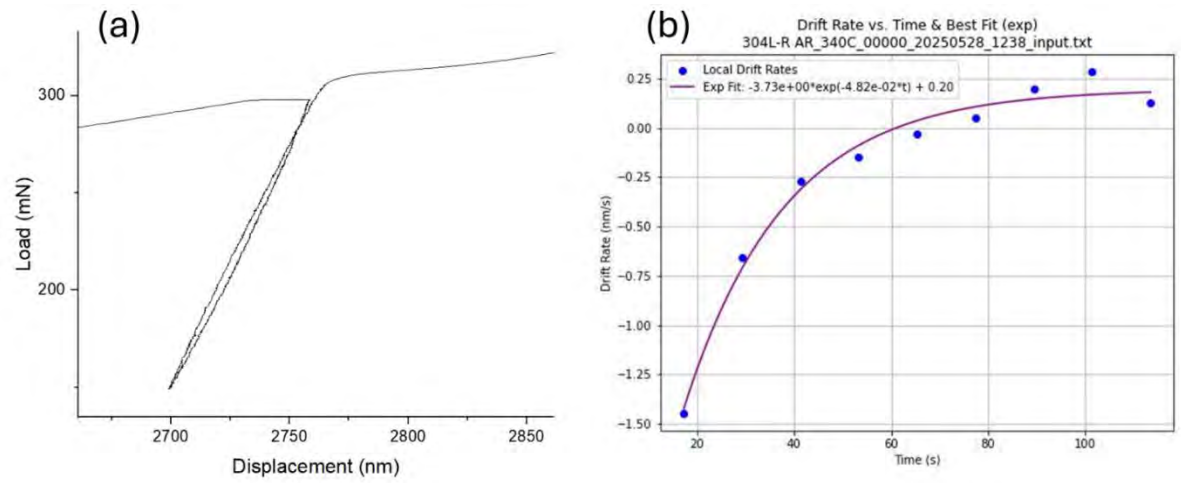

Figure 12. (a) Zoomed-in portion of an unloading and reloading segment, and (b) fitting of the drift rate between those segments.

2.2.4 Reduced modulus

The reduced modulus (E_r) is derived from the material's stiffness, which is calculated from the slope of the initial portion of the unloading curve[14]. For the experiments using the xSol high-temperature stage, the system compliance was calibrated at the beginning using a standard quartz sample. However, it was found that the compliance value changed each time the top plate was opened to replace a sample and then sealed again. Although efforts were made to apply a consistent clamping force, some variation in compliance persisted which affected the measurement of the reduced modulus. Consequently, the calculated reduced modulus values often deviated from known literature values due to either over- or under-correction of the system compliance (Fig. 13). This effect was particularly noticeable at high temperatures, where the data often showed artificially high modulus values due to over-correction. While manually adjusting the system compliance value could yield the expected E_r in the range of 150–220 GPa, this adjustment had no effect on the calculated hardness values. Although obtaining an accurate E_r is complementary to our objective, the main focus of this study is the hardness which was unaffected by this issue. Therefore, we proceeded with the existing settings due to time limitations on the TriboIndenter instrument.

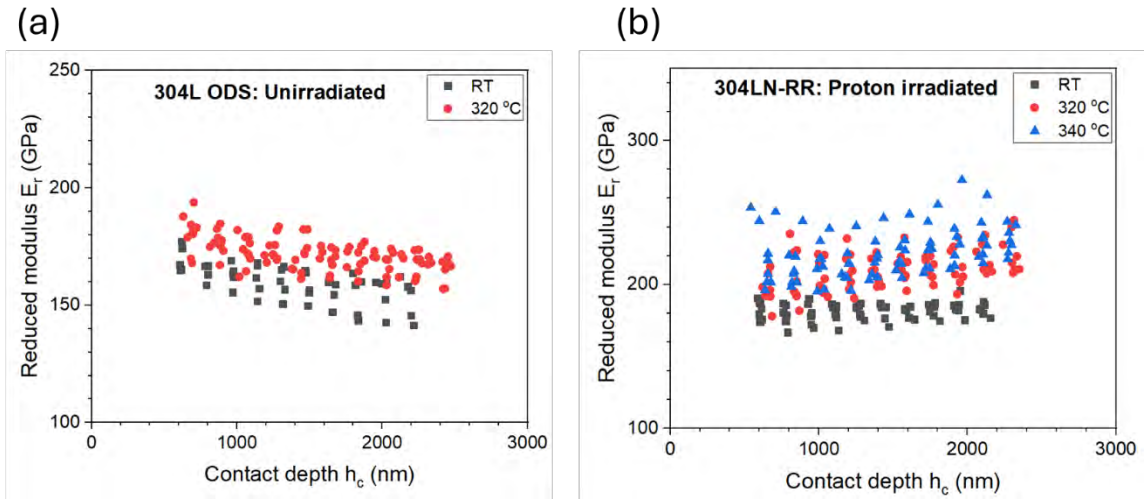

Figure 13. Examples of calculated reduced modulus as a function of contact depth for (a) unirradiated 304L ODS sample and (b) proton-irradiated 304LN-RR sample.

2.2.5 Hardness vs depth

Fig. 14 presents the hardness versus contact depth profiles for all unirradiated and irradiated specimens at both room and high temperatures. These profiles were derived from the analysis of unloading segments from the multiple-partial unloading technique. In general, the hardness decreases as the contact depth (h_c) increases, which is indicative of the ISE. For the unirradiated specimens at room temperature, all the wrought materials (Fig. 14a–14d) and the AM-HIP alloy (Fig. 14e) exhibited generally lower hardness values, while the UFG (Fig. 14f) and ODS (Fig. 14g) materials showed higher initial hardness. As expected, when the temperature was increased to 320 ºC and 340 ºC, a downward shift in the hardness values was observed for all materials. As observed in the 304L-UR data, no significant difference was observed between the hardness values at 320 ºC and 340 ºC.

For the proton-irradiated specimens at room temperature, the hardness values increased considerably for the 304LN-RR and AM-HIP alloys, which had initially lower hardness in their unirradiated condition. In the case of the proton-irradiated ODS material, there was only a slight increase in hardness from its already high unirradiated value. Consistent with the behavior of the unirradiated materials, increasing the temperature also resulted in a decrease in hardness for the proton-irradiated specimens. Similarly, no significant difference was observed between the hardness values measured at 320 ºC and 340 ºC for the irradiated specimens as seen for 304LN-RR.

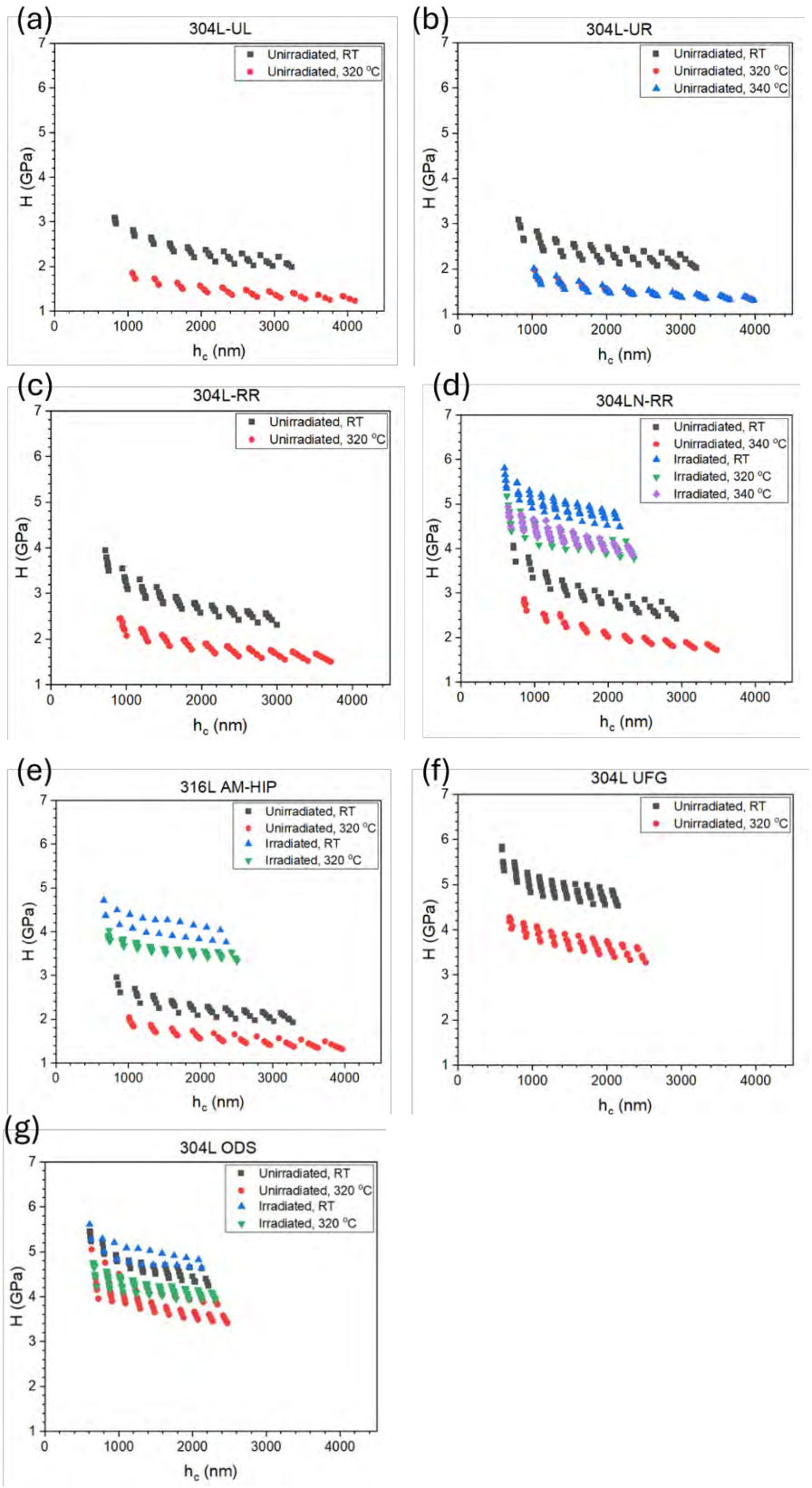

Figure 14. Hardness vs contact depth profiles for (a) 304L-UL, (b) 304L-UR, (c) 304L-RR, (d) 304LN-RR, (e) 316L AM-HIP, (f) 304L UFG, and (g) 304L ODS materials.

2.2.6 Bulk hardness

Bulk hardness (H_0) is the theoretical, depth-independent hardness at an infinite depth which is free from the influence of the ISE. The hardness versus contact depth results from Fig. 14 can be used to calculate the bulk hardness using the Nix-Gao model, which is described by the following equations:

$$\frac{H}{H_0} = \sqrt{1 + \frac{h^*}{h_c}}$$

$$H^2 = H_0^2 + \frac{H_0^2 h^*}{h_c}$$

where, H is the measured hardness at contact depth h_c, H_0 is the bulk hardness, and h^* is the characteristic length. The second rearranged equation allows for plotting H^2 vs $1/h_c$, and a linear fit of this plot yields a y-intercept from which the bulk hardness can be determined. Examples of such Nix-Gao analysis are provided in Fig. 15 for the unirradiated and irradiated 304LN-RR specimens at room and high temperature.

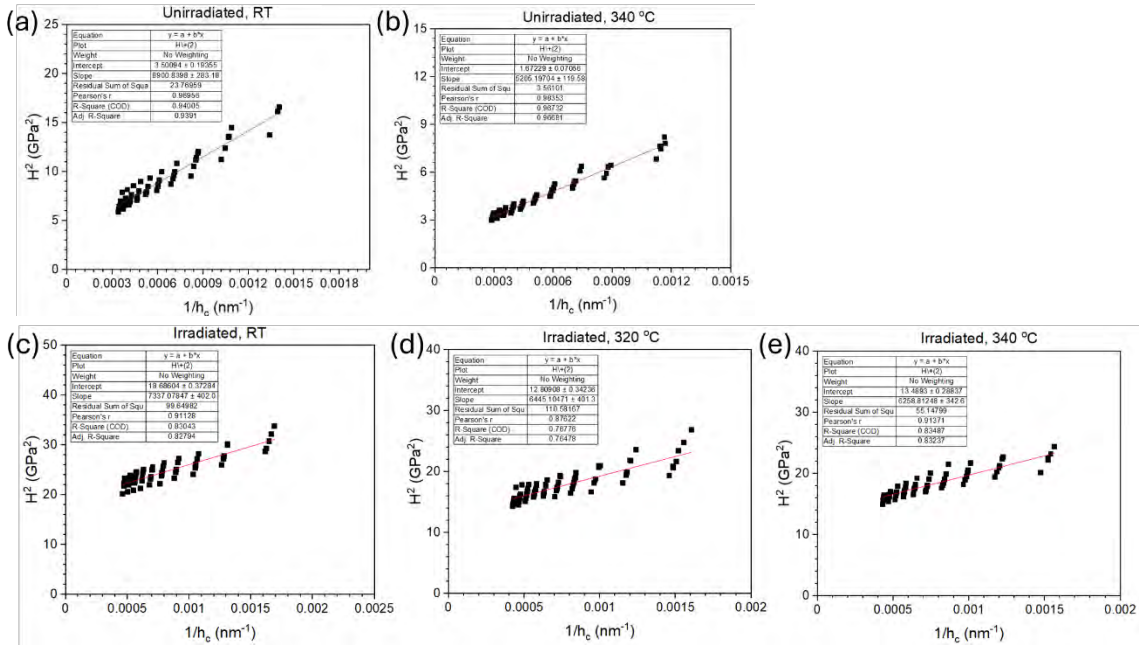

Figure 15. Nix-Gao analysis of 304LN-RR specimens under the following conditions: (a) Unirradiated at RT, (b) Unirradiated at 340 °C, (c) Irradiated at RT, (d) Irradiated at 320 °C, and (e) Irradiated at 340 °C.

Fig. 16 shows the plot of calculated H_0 values for all materials under all tested conditions, and the values are tabulated in Table 4 along with the percentage decrease at high temperature from their room temperature reference values. The trend is same as what's been observed from Fig. 14. The trends observed are consistent with the hardness-depth profiles shown in Fig. 14. At room temperature, the wrought and AM-HIP alloys exhibit a similar range of H_0 values, while the UFG and ODS alloys are much harder. In all cases, increasing the temperature decreases the H_0 values, whereas proton irradiation increases the H_0 values relative to the unirradiated state. The increase in H_0 due to proton irradiation is substantial for the wrought 304LN-RR and AM-HIP materials, while there is only a slight increase for the already hard ODS alloy. Increasing the temperature also decreases the H_0 values for the irradiated materials.

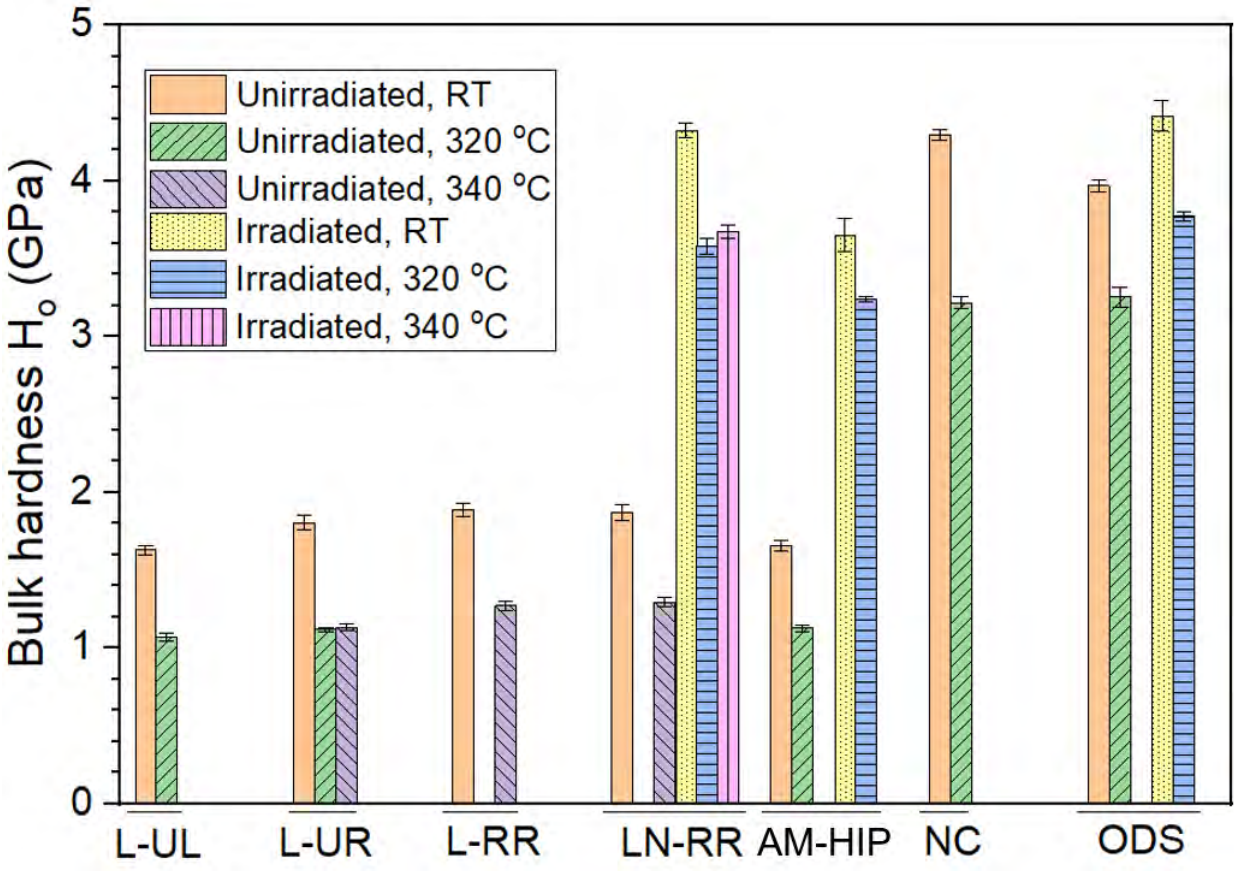

Figure 16. Summary of the calculated bulk hardness values of all materials under all tested conditions.

Table 4. Bulk hardness values and percentage decrease from their room temperature references.

Material	Bulk hardness (H_0, GPa)					
	Unirradiated (UI)			Proton-irradiated (PI)		
	RT	320 °C (% from UI-RT)	340 °C (% from UI-RT)	RT	320 °C (% from PI-RT)	340 °C (% from PI- RT)
304L-UL	1.63	1.07 (–34.4%)	–	–	–	–
304L-UR	1.80	1.12 (–38.0%)	1.13 (–37.4%)	–	–	–
304L-RR	1.88	–	1.27 (–32.6%)	–	–	–
304LN-RR	1.87	–	1.29 (–30.9%)	4.32	3.58 (–17.2%)	3.67 (–15.0%)
316L AM-HIP	1.66	1.12 (–32.1%)	–	3.65	3.24 (–11.2%)	–
304L UFG	4.29	3.21 (–25.1%)	–	–	–	–
304L ODS	3.97	3.25 (–18.0%)	–	4.41	3.77 (–14.6%)	–

2.2.7 Hardness – yield strength comparison

In the literature, correlations for unirradiated and irradiated austenitic stainless steels often use Vickers hardness (HV) data to determine the yield strength[16]. This data is typically obtained using high loads (often well above 300 gf), which removes the influence of the ISE. It is therefore reasonable to convert the calculated bulk hardness H_0 from this study to an equivalent HV. The HV derived from Berkovich instrumented indentation testing (IIT) is related to the bulk hardness by the expression $HV_{IIT} = 94.5H_0$[17].

Table 5 shows the experimental yield strength values for some of the materials used in this study and their percentage decrease relative to their room temperature reference values. The table also includes reference yield strength data for neutron-irradiated materials at similar temperatures. Interestingly for the wrought unirradiated materials, the percentage decrease in hardness at high temperature (31–38%) is comparable to the percentage decrease in yield strength (37–41%), although the decrease in hardness is slightly less pronounced (Fig. 17a). Similarly, the percentage decrease in hardness for the proton-irradiated materials in this study (11–17%) compares well with the decrease in yield strength reported for neutron-irradiated materials (11–15%) in Fig. 17b. In contrast, for the unirradiated UFG material, the percentage decrease in hardness (25%) is higher than that of its yield strength (16%), as shown in Tables 4 and 5.

This discrepancy for the UFG material can be explained by its stress-strain behavior at room temperature and 320 °C, shown in Fig. 18. The material's already low strain hardening behavior at room temperature degrades further at 320 °C, exhibiting considerable thermal softening in the plastic region. This results in a lower resistance to plastic deformation during micro-indentation at high temperatures, leading to a more substantial drop in hardness compared to the drop in yield strength. On the other hand, the strain hardening coefficients of conventional unirradiated austenitic stainless steels typically lie in a similar range and can even be slightly higher at 300–350 °C[18]. This could explain the observation for

the wrought alloys, where the decrease in hardness was largely comparable to, but slightly less than the decrease in yield strength. This means that the strain hardening coefficient is an important factor and should be considered for reliable hardness to yield-strength conversions, especially for engineered alloys that exhibit decreasing strain hardening behavior at high temperatures.

Existing correlations for the hardness–yield strength relationship in irradiated materials typically only consider the hardness and yield strength value[19]. However, Cahoon et al. offered an expression[19] that relates the Vickers hardness HV and yield strength σ_y with the strain hardening coefficient n:

$$\sigma_y = \frac{HV}{3} 0.1^n$$

Such a correlation has been reported to hold well for ferritic steel at temperatures up to 400 °C[20]. Furthermore, another of Cahoon's equations which correlates ultimate tensile strength with hardness and includes the strain hardening coefficient, has been shown to hold well for austenitic stainless steels at temperatures up to 1200 °C[21].

Applying this relationship to the wrought alloys in this study, a similar percentage drop in both hardness and yield strength is expected from Cahoon's relationship, assuming similar strain hardening coefficients at room temperature and at 320–340 °C. If the strain hardening coefficient is slightly higher at elevated temperatures, the percentage decrease in hardness would be slightly lower than that of the yield strength, as observed. For the UFG material, the lower strain hardening coefficient at higher temperatures results in a higher drop in hardness compared to the yield strength, which is also consistent with Cahoon's relationship and our observations. Therefore, further analysis is required to derive the strain hardening coefficient from the available tensile test and indentation results, and to confirm the applicability of Cahoon's correlation for irradiated materials at high temperatures.

Table 5. Experimental yield strength values and their percentage decrease from room temperature reference.

Irradiation condition	Material	Yield strength, MPa (% decrease from RT)			
		RT	320 °C	330 °C	340 °C
Unirradiated (this study)	304L-UL	279	176 (–36.9%)	–	–
	304L-UR	272	–	–	160 (–41.2%)
	304L-RR	321	–	–	197.5 (–38.5%)
	304LN-RR	309	–	–	194 (–37.2%)
	304L UFG	1085	910 (–16.1%)	–	–
Neutron-irradiated (references)	304/316 wrought	875, 875 [22]	740 (–15.4%) [23]	783 (–10.5%) [24]	–

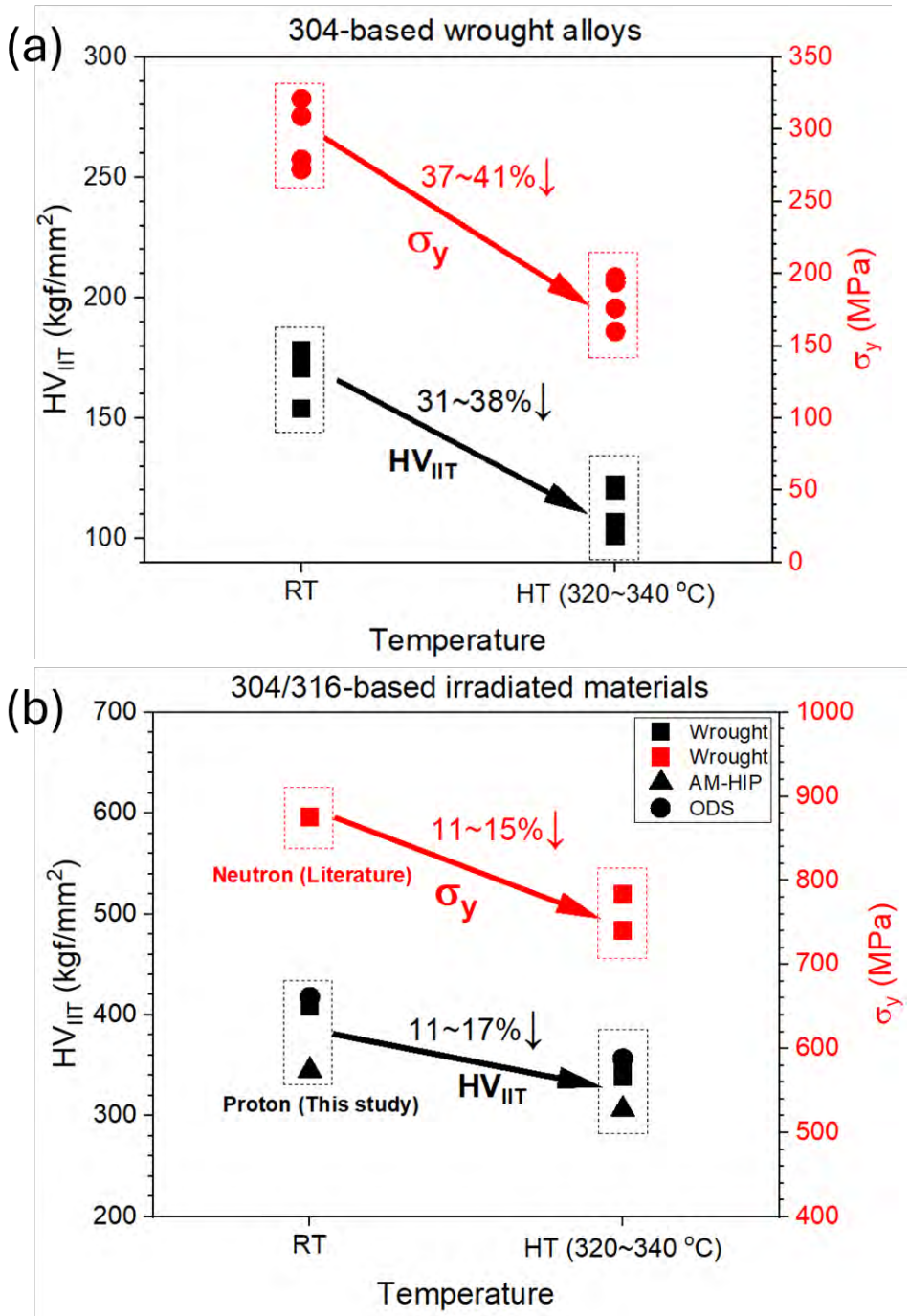

Figure 17. Comparison of hardness and yield strength evolution from room to high temperature for (a) unirradiated and (b) irradiated materials.

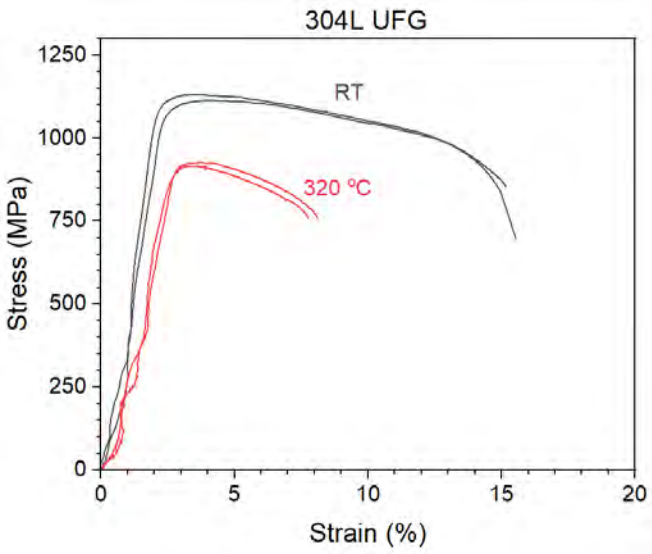

Figure 18. Engineering stress and strain behavior of unirradiated 304L UFG at room temperature and 320 °C.

3. IASCC Testing

3.1 Experiment

3.1.1 Irradiated Materials Testing Laboratory

The Irradiated Materials Testing Laboratory (IMTL) at the University of Michigan is equipped with multiple autoclave systems designed for testing irradiated materials in aqueous environments. The 4PB IASCC tests for the scoped work will be conducted in parallel using the IM2 and IM3/IM5 systems. The IASCC tests will be performed in a simulated PWR water chemistry environment at 320 °C and 2000 psi. The pictures and schematic of the IM2 test loop are shown in Figs. 19 & 20.

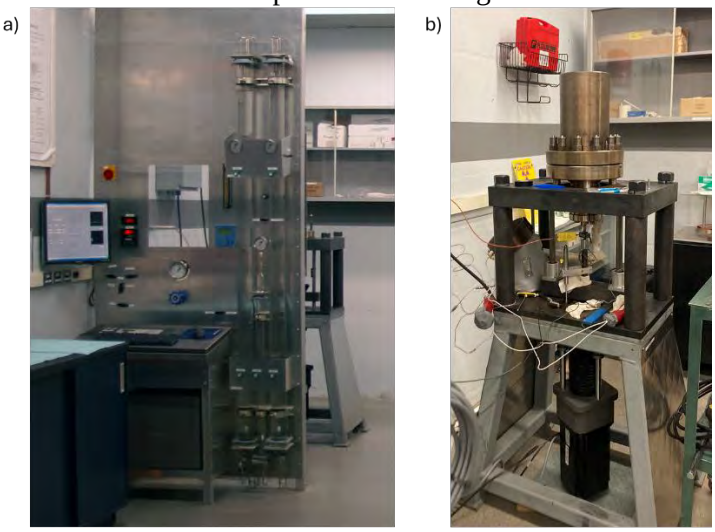

Figure 14: a) IM2 front panel with main and makeup columns and b) IM2 autoclave and motor system.

IM2

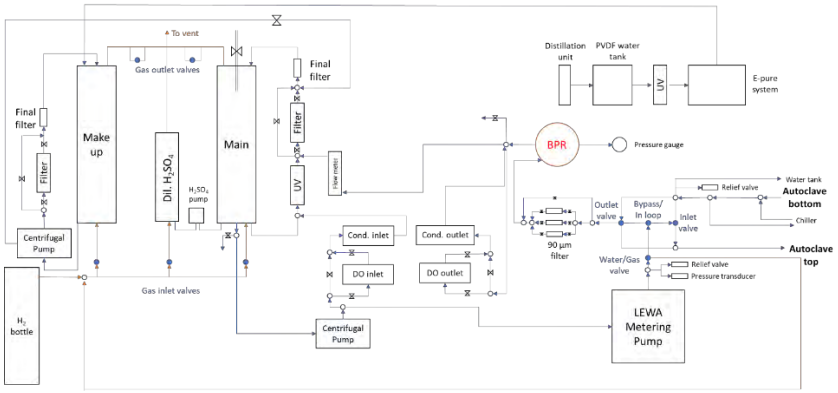

Figure 20: Irradiated Materials System 2 (IM2) diagram.

During the experiments, the main column will be filled with PWR water with 1000 ppm B (as H_3BO_3) and 2 ppm Li (as LiOH). This water chemistry corresponds to a pH of 6.5 and conductivity of 21.5 µS/cm, which will be monitored throughout the test. A hydrogen overpressure will be maintained in the main column to achieve a dissolved hydrogen concentration of 35 cc/kg. The main column water will be continuously circulated through an ion exchange filter saturated with borate and Li cations, which will be used to remove ionic impurities. A custom LabView code will monitor, control, and record all experimental parameters during testing.

3.1.2 Four-Point Bend Fixture

The 4PB test was recently developed for IASCC initiation studies, particularly suited for neutron-irradiated samples where limited material volume and availability are common [9,25–28]. This test generates an area (0.5 x 3.5 mm) of nearly uniaxial tensile stress and strain in the central region of the sample (Fig. 4), promoting multiple crack initiation sites within a single specimen. The primary objective is to determine the fraction of irradiated yield strength at which the material becomes susceptible to IASCC initiation. To achieve this, interrupted loading steps will be conducted, whereby the sample is sealed in the PWR environment and incrementally loaded below the irradiated yield stress, followed by periodic unloading for crack inspection using scanning electron microscopy (SEM).

The schematic diagram of the 4PB test setup is shown in Fig. 21. Two fixture assemblies were fabricated to allow parallel testing in two autoclave systems (IM2 and IM3/IM5). The setup comprises an upper-loading punch with two closely spaced indents and a lower sample support. The sample is carefully positioned at the center of the fixture using non-metallic tweezers, ensuring that the proton-irradiated surface, which is susceptible to IASCC, faces downward. Centering pins are used to position the sample precisely. A photograph is taken to verify that the indents are aligned with the center of the sample and to ensure consistent placement during subsequent incremental loading. The upper-loading punch contacts the opposite side of the sample and moves downward to apply the load, causing the sample to bend convexly on the downward-facing irradiated surface. The 4PB tests will start with loading up to 40% of the irradiated yield strength, followed by 10% load increments until crack initiation is observed. Most fixture components were fabricated from 316 SS material, while the critical load-transferring parts, including the upper-loading punch and sample support, were made from solution-annealed Inconel 718. The Inconel 718 components were age-treated at 720°C for 8 hours, followed by 620°C for 10 hours in an argon environment. As a result of the aging treatment, the hardness of these components increased from 220 HV0.5 to 524 HV0.5.

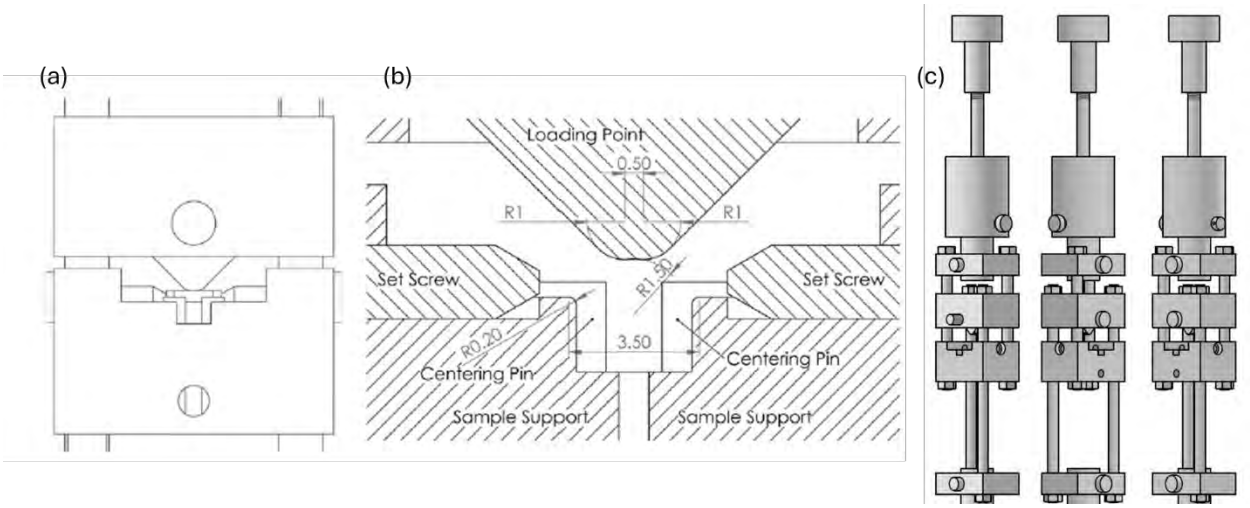

Figure 21: (a) Schematic, (b) cross-section view of the 4PB loading fixture [9] and (c) computer-aided design (CAD) drawing of the fully assembled loading fixture.

3.1.3 Procedure

The 4PB sample was carefully loaded into the test fixture and aligned to ensure consistent positioning between loading steps. The autoclave was sealed, filled with PWR water, pressurized to 2000 psi, and heated to 320 °C. Once the system stabilized under the test conditions, the test fixture's pull rod was connected to a crosshead driven by a stepping motor. The motor was programmed to lower the crosshead, dynamically straining the 4PB sample surface at a strain rate of 4×10^{-8} /s. The initial step involved loading from 0% to 40% of the irradiated yield strength of the sample, after which the sample was unloaded once the target stress was reached. The load corresponding to the target surface stress value was determined by the FEA simulation.

After the autoclave was cooled to room temperature, the sample was removed for crack examination. Examination will be confined to a uniformly strained central region measuring 0.5 × 3.5 mm, previously identified by indent marks on the irradiated side of the sample. A JEOL JSM-6480 scanning electron microscope (SEM) in backscattered electron (BSE) mode will inspect the sample for cracks at 1000X magnification. If no cracks are detected, the sample will be reloaded at an additional 10% of the irradiated yield strength under the same experimental conditions. This process will be repeated until cracking is observed. The location of observed cracks will be documented to correlate with previous loading steps and to identify any microstructural features preceding crack formation. Detailed statistical analysis will be performed on the cracking behavior, and the fraction of irradiated yield strength at which cracking occurs will be used to compare IASCC susceptibility between stainless steels with novel microstructures. High-resolution transmission electron microscopy (TEM) will be conducted at the crack tip regions to investigate the grain boundary oxide formation, microstructural characteristics, and factors contributing to IASCC initiation.

3.2 Results

Three locations on the wrought 304L sample exhibited IASCC cracks at 60% YS, as diagrammed in (Fig. 22). All three cracks are nearly perpendicular to the applied tensile stress and appeared at oxidized GBs. The progression of these cracks under backscatter electron (BSE) microscopy is shown in (Figs. 23-25), opening up from 40% YS to cracking at 60% YS. A final photo in secondary electron mode (SE) was taken to visualize the cracking behavior.

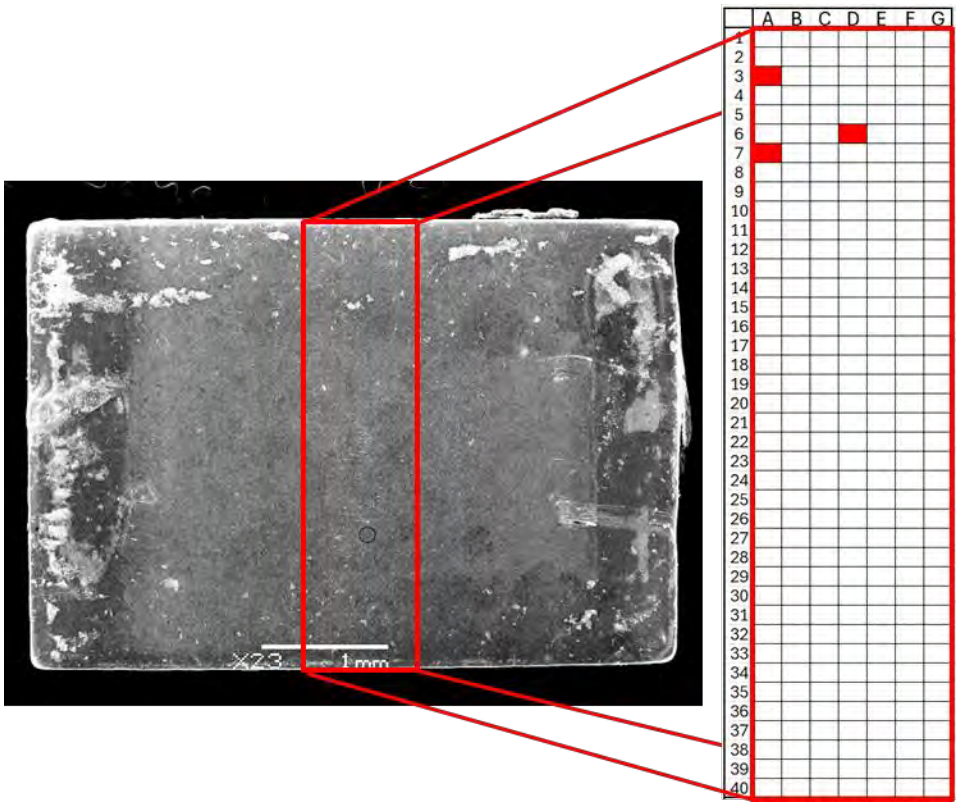

Figure 22: Crack locations on a wrought 304L SS sample loaded to 60% YS.

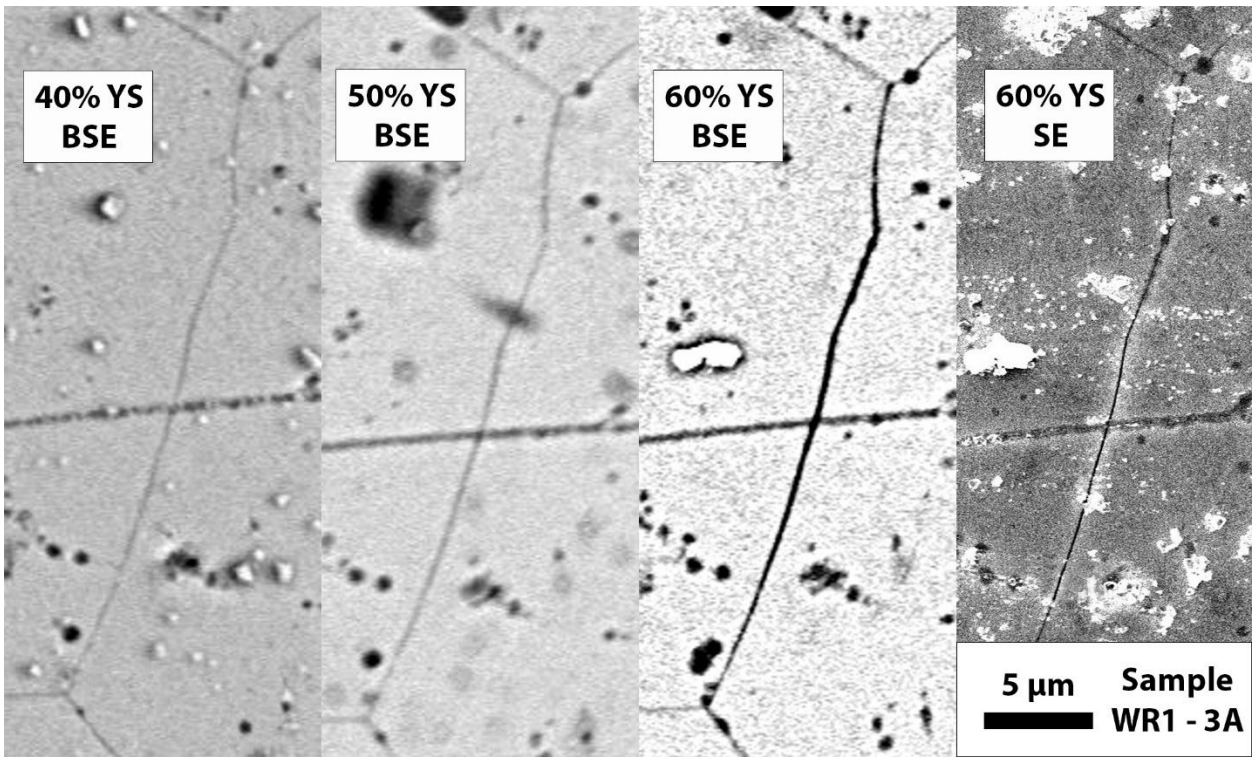

Figure 23: IASCC crack progression with increasing stress at site 3A

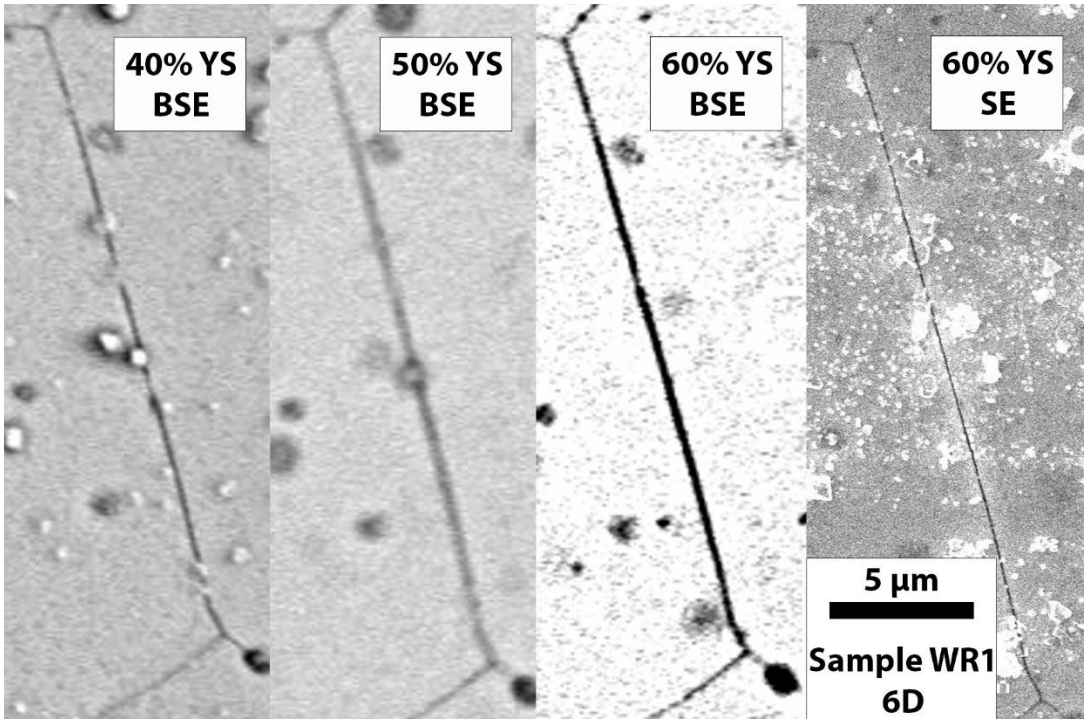

Figure 24: IASCC crack progression with increasing stress at site 6D.

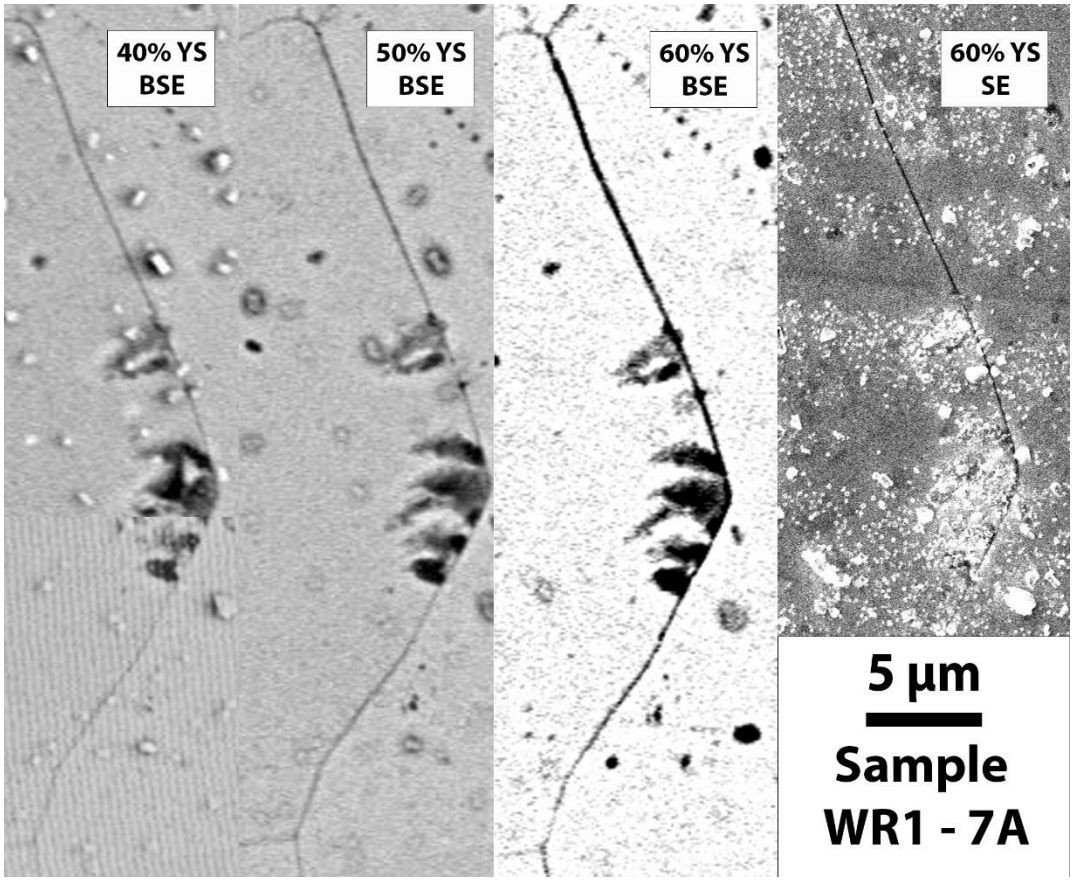

Figure 25: IASCC crack progression with increasing stress at site 7A.

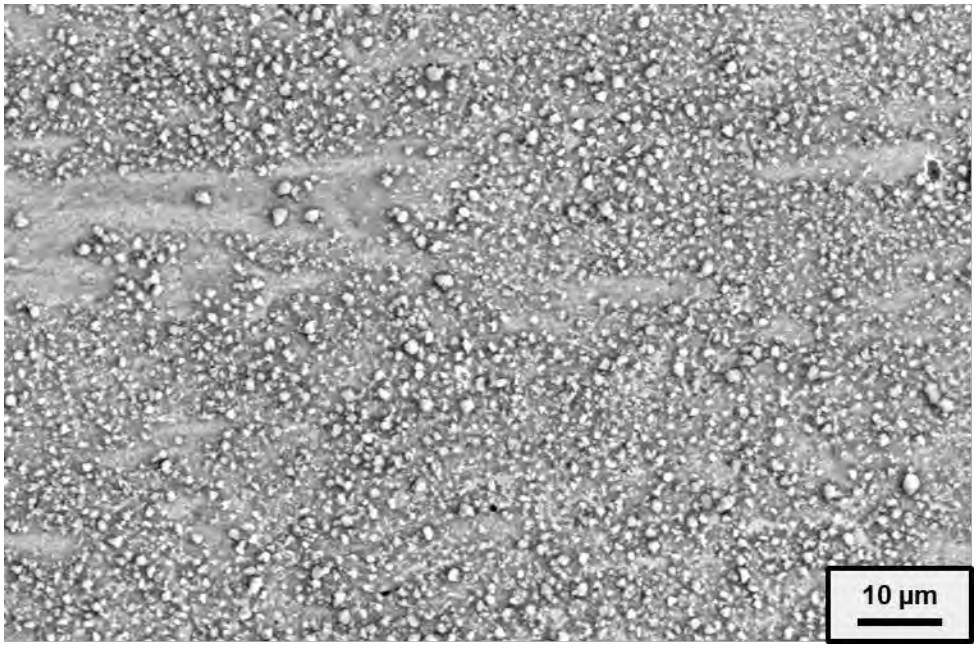

Figure 26: Oxidized surface of ODS sample after 4PB test.

In contrast, the ODS sample did not exhibit any cracks after loading it to 45 lbs, which is 15 lbs greater than the 60% YS condition for the WR sample (Fig. 26).

3.3 Discussion

The wrought sample behaved consistently with previous literature, where IASCC can occur around 60-70% YS. All three crack locations showed the expected preliminary signs of cracking: oxidized GB perpendicular to the applied stress. Notably, dislocation channels were not visible on the surface of the sample. Two explanations can confront this unexpected finding: either dislocation channels are not visible due to imaging or surface roughness, or dislocation channels were not involved in the initiation of these cracks.

The ODS sample has shown low susceptibility to crack formation at this point in testing. Continued loading, combined with FEA to calculate the local stress condition, will allow us to determine if cracking occurs after 100% YS is reached. Dislocation channels will be difficult to distinguish on this surface, due to the high oxidation present. While testing is still preliminary, the ODS microstructure has demonstrated a promising durability to the conditions that produced cracks in the wrought microstructure

4. Manufacture of New Powder Materials

In this study, we have designed 316L ODS steel by mechanical alloying, followed by spark plasma sintering. An initial study has been carried out to optimize the milling time and temperature. 1 wt.% nano-size Y_2O_3 was added to the 316L stainless steel powder and milled for 10 hours and the changes in the particle morphology, super-saturated solid solution of Y and O in the 316L matrix, and formation of dispersoids while consolidated using SPS were analyzed. The effect of milling Y_2O_3 addition to the matrix was observed by the change in the microstructure and mechanical properties.

4.1 Mechanical alloying 316L SS with addition of Y_2O_3

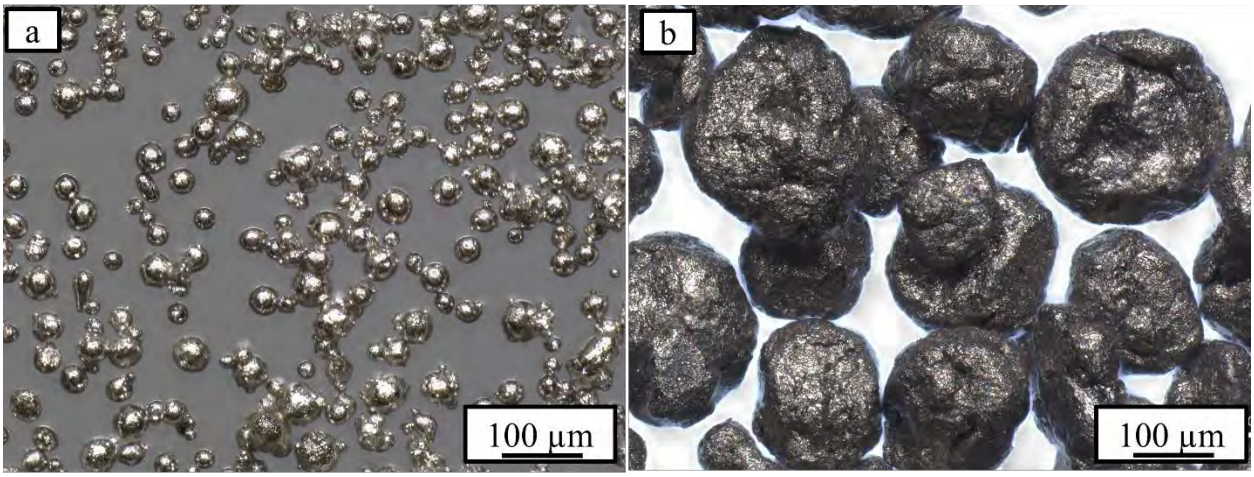

Figure 27: (a) As-received powder, (b) Milled powder.

316L austenitic stainless steel (SS) powder was reinforced with nano-sized Y_2O_3 particulates (average particle size: 20–30 nm) through mechanical milling using a Pulverisette 7 high-energy planetary ball mill. Milling was performed for 10 h at a rotational speed of 700 rpm under an inert argon atmosphere to prevent oxidation and contamination.

As shown in Figure 27a, the as-received 316L powder particles exhibited a predominantly spherical morphology with a smooth and reflective surface, characteristic of gas-atomized powders. Following mechanical milling (Figure 27b), the particles developed a flatter, irregular morphology with a darker appearance, indicative of surface roughening and contamination-free oxide dispersion incorporation.
During milling, the repeated high-energy impacts between the milling media and the powder particles induced severe plastic deformation. This deformation led to work hardening, an increase in dislocation density, and the accumulation of significant lattice strain within the particles. The nanometric Y_2O_3 particulates were progressively embedded and uniformly dispersed within the steel matrix via a cold welding–fracturing–rewelding cycle, enhancing the likelihood of grain refinement and eventual oxide dispersion strengthening during subsequent consolidation processes.

4.2 Characterization of an as-received powder particle

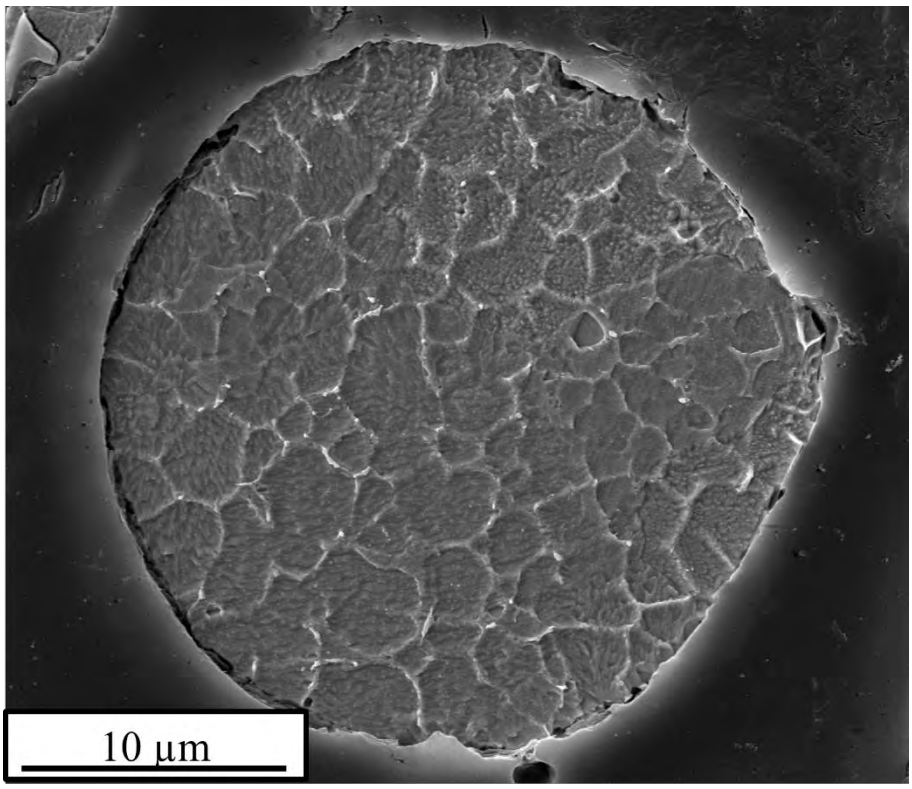

Figure 28: Shows the grain size of the as-received 316L powder particles.

Figure 28 shows the grain size of the as-received 316L powder particles. The powder particles were hardened in the epoxy and polished using emery paper, followed by cloth polishing. The mirror-polished sample was subjected to the etchant to reveal the grain. Aqua regia was used as an etchant solution. The grain size of the as-received sample was found to be ~3 µm.

4.3 TEM characterization of ball-milled particles

Figure 29 shows a TEM micrograph of a mechanically alloyed 316L stainless steel powder particle with nano-sized Y_2O_3 additions. The microstructural analysis reveals an absence of distinct regions containing both yttrium (Y) and oxygen (O) in their original stoichiometric proportions. This observation suggests that during high-energy ball milling, the Y_2O_3 nanoparticles underwent mechanical fragmentation and chemical dissociation, resulting in the breakdown of the oxide into its constituent elements. The liberated Y and O atoms were subsequently incorporated into the stainless steel matrix, leading to the formation of a supersaturated solid solution far beyond the equilibrium solubility limits.

This phenomenon is consistent with the underlying principles of mechanical alloying (MA), a solid-state powder metallurgy technique involving the cyclic sequence of cold welding, fracturing, and rewelding of powder particles under repeated high-energy impacts. The extreme plastic deformation generated during MA produces a high density of lattice defects, including dislocations, vacancies, and grain boundaries, which act as short-circuit diffusion pathways for solute atoms. Such a defect-rich environment significantly enhances atomic mobility even at ambient temperature, facilitating:

1. Nanocrystalline Microstructure Formation through grain subdivision and dynamic recovery at the nanoscale.

2. Alloying of Thermodynamically Immiscible Elements via Non-Equilibrium Solid-State Diffusion.

3. Extension of Solid Solubility Limits well beyond equilibrium values due to the combined effects of high defect density and mechanical energy input.

In the present case, the dissociation of Y_2O_3 and subsequent incorporation of Y and O into the steel lattice is expected to promote oxide dispersion strengthening (ODS) upon consolidation and thermal treatment, as fine oxide precipitates can re-form within the matrix.

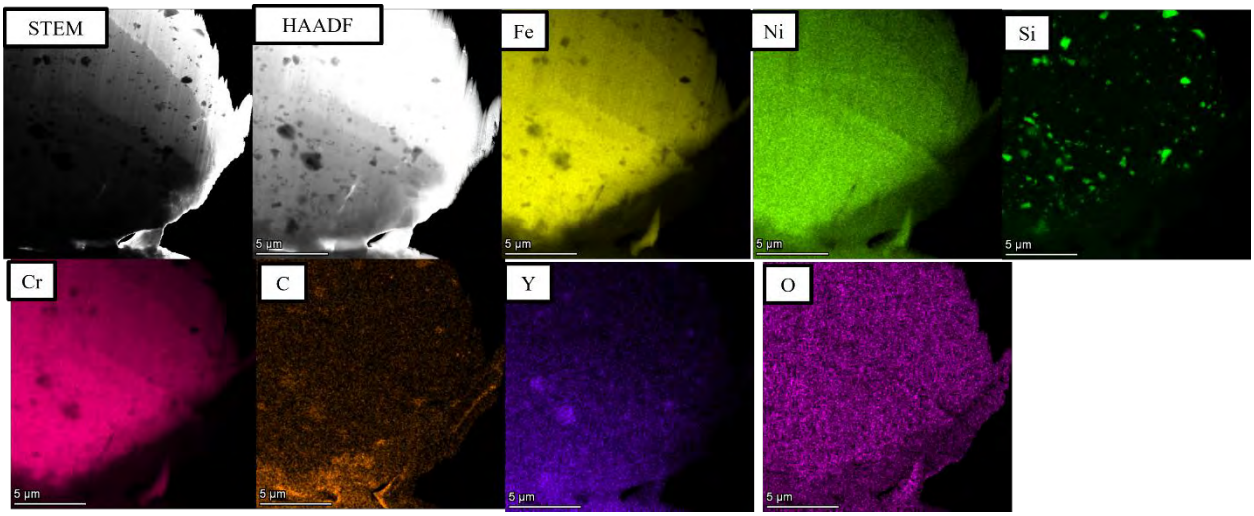

Figure 29: Shows the TEM elemental mapping image of a ball-milled powder particle.

In addition, silicon (Si) and chromium (Cr) present in the alloy are also likely to participate in carbide formation due to their strong thermodynamic affinity for carbon. This is supported by the high negative Gibbs free energy of formation for chromium carbides (e.g., $Cr_{23}C_6$, Cr_7C_3) and silicon carbides (SiC), which indicates a strong driving force for their precipitation during thermal exposure or consolidation. The preferential bonding of carbon with Cr and Si can occur either at grain boundaries or within the matrix, potentially influencing grain boundary cohesion, precipitation hardening, and high-temperature stability of the alloy.

4.4 Characterization of consolidated samples

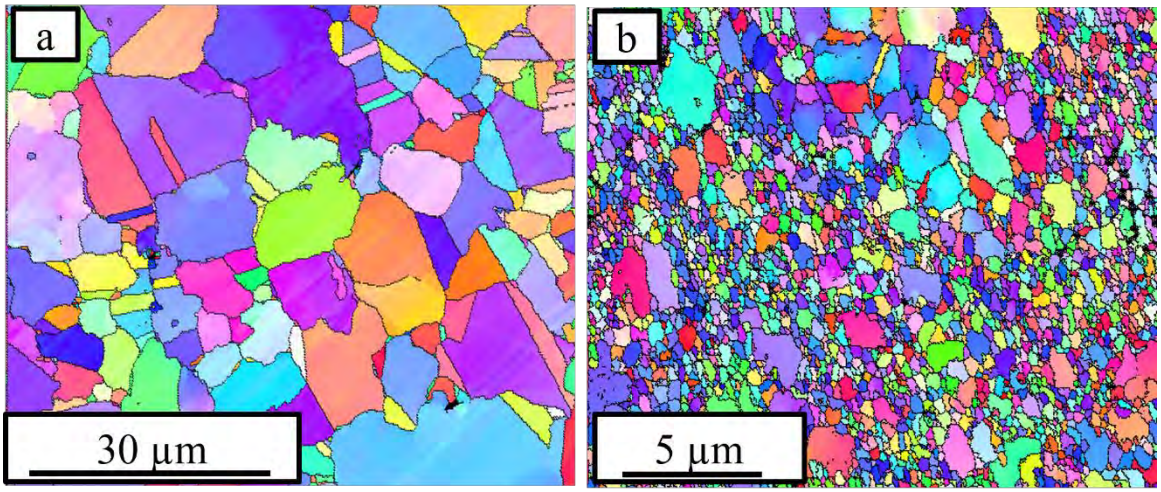

Figure 30: Microstructure of SPSed (a) As-received 316L and (b) Y_2O_3 added ball milled sample

Figures 30a and 30b show the microstructure of the SPS 316L as received and the Y_2O_3 added ball-milled sample, respectively. The as-received sample was found with an estimated grain size of 10 µm. On

the other hand, the Y_2O_3 added ball milled sample was found with a grain size of ~0.7 µm. There is an estimated 93% of grain size reduction. The reduction of the grain size is the attribute of Y_2O_3 addition, which takes part in the formation of stable dispersoids. These are acting as a barrier to grain growth. Apart from this, the dislocation density also takes part in grain refinement.

Vickers hardness was measured on both samples. The as-received sample had a Vickers hardness of **370±17 HV**, while the Y_2O_3 added ball milled sample had a hardness of **540±23 HV**. The increase in hardness could be due to Grain size strengthening, dispersion strengthening, and/or dislocation strengthening.

5. Conclusions

- Proton-irradiated specimens were evaluated by an incremental four-point bend (4PB) tests to qualify IASCC initiation susceptibility by the fraction of irradiated yield strength (%YS) at which cracks first appear. Accurate surface stress determination during bending requires finite-element analysis (FEA), which in turn depends on reliable values for the 320ºC yield strength of both the thin irradiated layer and the unirradiated bulk.
- To provide the yield strength at high temperature and in the irradiated condition for alloys with engineered microstructures, instrumented micro-indentation with a diamond Berkovich probe was conducted at room temperature and high temperatures (320 ºC and 340 ºC). A multiple-partial-unloading technique provided hardness as a function of penetration depth, from which bulk hardness values were determined.
- The percentage decrease in hardness from room temperature to higher temperature closely matched the decrease in yield strength for wrought unirradiated alloys.
- In proton-irradiated specimens, the hardness decrease was similar to the decrease in yield strength data obtained from reference for neutron-irradiated materials. In contrast, the unirradiated ultrafine-grained alloy exhibited a markedly higher hardness drop, attributed to its lower work hardening capacity and greater thermal softening at higher temperatures.
- IASCC experiments were conducted on wrought 304L samples irradiated to 5 dpa, and they were found to crack at 60% of their unirradiated yield strength.
- 316L ODS containing 1 wt.% Y_2O_3 was successfully synthesized with high-energy mechanical alloying, ensuring homogeneous distribution of oxide particles within the metal matrix.
- The ODS alloy showed a grain size reduction of 93% compared to the initial 316L microstructure and a Vickers hardness increase of approximately 46%
- TEM analysis confirms the formation of a supersaturated solid solution, attributed to the dissociation of Y_2O_3 and subsequent incorporation of Y and O atoms into the matrix during milling. The presence of Y_2O_3 is expected to facilitate the formation of thermodynamically stable oxide dispersoids upon consolidation and heat treatment.

6. References

[1] N. Hashimoto, S.J. Zinkle, A.F. Rowcliffe, J.P. Robertson, S. Jitsukawa, Deformation mechanisms in 316 stainless steel irradiated at 60°C and 330°C, Journal of Nuclear Materials 283–287 (2000) 528–534. https://doi.org/10.1016/S0022-3115(00)00087-8.

[2] M.D. McMurtrey, G.S. Was, L. Patrick, D. Farkas, Relationship between localized strain and irradiation assisted stress corrosion cracking in an austenitic alloy, Materials Science and Engineering: A 528 (2011) 3730–3740. https://doi.org/10.1016/j.msea.2011.01.073.

[3] D.C. Johnson, B. Kuhr, D. Farkas, G.S. Was, Quantitative linkage between the stress at dislocation channel – Grain boundary interaction sites and irradiation assisted stress corrosion crack initiation, Acta Materialia 170 (2019) 166–175. https://doi.org/10.1016/j.actamat.2019.02.032.

[4] B. Kuhr, D. Farkas, I.M. Robertson, D. Johnson, G. Was, Stress Localization Resulting from Grain Boundary Dislocation Interactions in Relaxed and Defective Grain Boundaries, Metall Mater Trans A 51 (2020) 667–683. https://doi.org/10.1007/s11661-019-05534-0.

[5] H. Dugdale, D.E.J. Armstrong, E. Tarleton, S.G. Roberts, S. Lozano-Perez, How oxidized grain boundaries fail, Acta Materialia 61 (2013) 4707–4713. https://doi.org/10.1016/j.actamat.2013.05.012.

[6] G.S. Was, C.-B. Bahn, J. Busby, B. Cui, D. Farkas, M. Gussev, M. Rigen He, J. Hesterberg, Z. Jiao, D. Johnson, W. Kuang, M. McMurtrey, I. Robertson, A. Sinjlawi, M. Song, K. Stephenson, K. Sun, S. Swaminathan, M. Wang, E. West, How irradiation promotes intergranular stress corrosion crack initiation, Progress in Materials Science 143 (2024) 101255. https://doi.org/10.1016/j.pmatsci.2024.101255.

[7] Z. Jiao, G.S. Was, Impact of localized deformation on IASCC in austenitic stainless steels, Journal of Nuclear Materials 408 (2011) 246–256. https://doi.org/10.1016/j.jnucmat.2010.10.087.

[8] J. Yang, L. Hawkins, Z. Shang, E.A. McDermott, B.K. Tsai, L. He, Y. Lu, M. Song, H. Wang, X. Lou, Dislocation channel broadening–A new mechanism to improve irradiation-assisted stress corrosion cracking resistance of additively manufactured 316 L stainless steel, Acta Materialia 266 (2024) 119650. https://doi.org/10.1016/j.actamat.2024.119650.

[9] K.J. Stephenson, G.S. Was, The role of dislocation channeling in IASCC initiation of neutron irradiated stainless steel, Journal of Nuclear Materials 481 (2016) 214–225. https://doi.org/10.1016/j.jnucmat.2016.09.001.

[10] X. Yan, X. Zhang, F. Wang, T. Stockdale, Y. Dzenis, M. Nastasi, B. Cui, Fabrication of ODS Austenitic Steels and CoCrFeNi High-Entropy Alloys by Spark Plasma Sintering for Nuclear Energy Applications, JOM 71 (2019) 2856–2867. https://doi.org/10.1007/s11837-019-03531-7.

[11] C. Sun, S. Zheng, C.C. Wei, Y. Wu, L. Shao, Y. Yang, K.T. Hartwig, S.A. Maloy, S.J. Zinkle, T.R. Allen, H. Wang, X. Zhang, Superior radiation-resistant nanoengineered austenitic 304L stainless steel for applications in extreme radiation environments, Sci Rep 5 (2015) 7801. https://doi.org/10.1038/srep07801.

[12] Mechanical Grinding and Polishing, (n.d.). https://doi.org/10.31399/asm.hb.v09.9781627081771.

[13] W.D. Nix, H. Gao, Indentation size effects in crystalline materials: A law for strain gradient plasticity, Journal of the Mechanics and Physics of Solids 46 (1998) 411–425. https://doi.org/10.1016/S0022-5096(97)00086-0.

[14] W.C. Oliver, G.M. Pharr, An improved technique for determining hardness and elastic modulus using load and displacement sensing indentation experiments, Journal of Materials Research 7 (1992) 1564–1583. https://doi.org/10.1557/JMR.1992.1564.
[15] K.I. Schiffmann, R.L.A. Küster, Comparison of hardness and Young's modulus by single indentation and multiple unloading indentation, International Journal of Materials Research 95 (2004) 311–316. https://doi.org/10.1515/ijmr-2004-0067.
[16] J.T. Busby, M.C. Hash, G.S. Was, The relationship between hardness and yield stress in irradiated austenitic and ferritic steels, Journal of Nuclear Materials 336 (2005) 267–278. https://doi.org/10.1016/j.jnucmat.2004.09.024.
[17] D.L. Krumwiede, T. Yamamoto, T.A. Saleh, S.A. Maloy, G.R. Odette, P. Hosemann, Direct comparison of nanoindentation and tensile test results on reactor-irradiated materials, Journal of Nuclear Materials 504 (2018) 135–143. https://doi.org/10.1016/j.jnucmat.2018.03.021.
[18] R.K. Desu, H. Nitin Krishnamurthy, A. Balu, A.K. Gupta, S.K. Singh, Mechanical properties of Austenitic Stainless Steel 304L and 316L at elevated temperatures, Journal of Materials Research and Technology 5 (2016) 13–20. https://doi.org/10.1016/j.jmrt.2015.04.001.
[19] J.R. Cahoon, W.H. Broughton, A.R. Kutzak, The determination of yield strength from hardness measurements, Metall Trans 2 (1971) 1979–1983. https://doi.org/10.1007/BF02913433.
[20] C. Hsu, Correlation of hot-microhardness with elevated-temperature tensile properties of low activation ferritic steel, Journal of Nuclear Materials 141–143 (1986) 518–522. https://doi.org/10.1016/S0022-3115(86)80093-9.
[21] J. Moteff, R.K. Bhargava, W.L. McCullough, Correlation of the hot-hardness with the tensile strength of 304 stainless steel to temperatures of 1200°C, Metall Trans A 6 (1975) 1101–1104. https://doi.org/10.1007/BF02661365.
[22] S.A. Maloy, M.R. James, W.R. Johnson, T.S. Byun, K. Farrell, M.B. Toloczko, Comparison of fission neutron and proton/spallation neutron irradiation effects on the tensile behavior of type 316 and 304 stainless steel, Journal of Nuclear Materials 318 (2003) 283–291. https://doi.org/10.1016/S0022-3115(03)00087-4.
[23] Y. Chen, W. Soppet, B. Alexandreanu, K. Natesan, Technical Letter Report of Slow-Strain-Rate Tensile Tests on Irradiated Stainless Steels in a PWR Environment, 2013. https://doi.org/10.2172/1104657.
[24] CIR II Program: Description of the Boris 6 Experiment in the BOR-60 Fast Breeder Reactor, (n.d.). https://www.epri.com/research/products/000000000001009418 (accessed August 22, 2025).
[25] D. Du, K. Sun, G.S. Was, IASCC of neutron irradiated 316 stainless steel to 125 dpa, Materials Characterization 173 (2021) 110897. https://doi.org/10.1016/j.matchar.2021.110897.
[26] K. Chen, M.R. Ickes, M.A. Burke, G.S. Was, The effect of potassium hydroxide primary water chemistry on the IASCC behavior of 304 stainless steel, Journal of Nuclear Materials 558 (2022) 153323. https://doi.org/10.1016/j.jnucmat.2021.153323.
[27] S. Swaminathan, K. Sun, G.S. Was, Decoupling the roles of grain boundary oxidation and stress in IASCC of neutron-irradiated 304L stainless steel, Journal of Nuclear Materials 585 (2023) 154604. https://doi.org/10.1016/j.jnucmat.2023.154604.

[28] A.S. Sinjlawi, L. Dong, M. Ickes, K. Sun, G.S. Was, Irradiation assisted stress corrosion cracking of 347 stainless steel in simulated PWR primary water containing lithium hydroxide or potassium hydroxide, Journal of Nuclear Materials 586 (2023) 154676. https://doi.org/10.1016/j.jnucmat.2023.154676.